A 14.5 million-year record of East Antarctic Ice Sheet fluctuations from the central Transantarctic Mountains, constrained with cosmogenic ^{3}He, ^{10}Be, ^{21}Ne, and ^{26}Al

Allie Balter[1,2], Gordon Bromley[2,3], Greg Balco[4], Holly Thomas[1], Margaret S. Jackson[3]

[1]School of Earth and Climate Sciences, University of Maine, Orono, Maine, USA

[2]Climate Change Institute, University of Maine, Orono, Maine, USA

[3]Geography, National University of Ireland, Galway, Ireland

[4]Berkeley Geochronology Center, Berkeley, California, USA

Correspondence to: Allie Balter (abalter@ldeo.columbia.edu)

Abstract. The distribution of moraines in the Transantarctic Mountains affords direct constraint of past ice-marginal positions of the East Antarctic Ice Sheet (EAIS). Here, we describe glacial-geologic observations and cosmogenic-nuclide exposure ages from Roberts Massif, an ice-free area in the central Transantarctic Mountains. We measured cosmogenic ^{3}He, ^{10}Be, ^{21}Ne, and ^{26}Al in 180 dolerite and sandstone boulders collected from 24 distinct deposits. Our data show that a cold-based EAIS was present, in a configuration similar to today, for many periods over the last ~14.5 Myr, including the mid-Miocene, Late Pliocene, and early-to-mid Pleistocene. Moraine ages at Roberts Massif increase with distance from, and elevation above the modern ice margin, which is consistent with a persistent EAIS extent during glacial maxima, and slow, isostatic uplift of the massif itself in response to trough incision by outlet glaciers. We also employ the exceptionally high cosmogenic-nuclide concentrations in several boulders, along with multi-isotope measurements in sandstone boulders, to infer extremely low erosion rates (<< 5 cm/Myr) over the period covered by our record. Although our data are not a direct measure of ice volume, the Roberts Massif glacial record indicates that the EAIS was present and similar to its current configuration during at least some periods when global temperature was believed to be warmer and/or atmospheric CO_2 concentrations were likely higher than today.

1 Introduction

In this paper, we describe glacial deposits preserved in the central Transantarctic Mountains (TAM, Figure 1) that provide unambiguous evidence for the presence of the East Antarctic Ice Sheet (EAIS), in a configuration similar to today, for periods of the middle Miocene, late Pliocene, and early to middle Pleistocene. Our chronology therefore provides geologic targets for ice volume reconstructions derived from marine proxy records and sea-level estimates. Current estimates of pre-Pleistocene EAIS ice volume are based largely on δ^{18}O of benthic foraminifera (e.g., Shevenell et al., 2008), which primarily records global temperature and ice volume, and farfield sea-level indicators (e.g., Miller et al., 2005), such as raised shorelines (e.g., Rovere et al., 2014). These proxy records (e.g., Holbourn et al., 2013), along with stratigraphic evidence from ice proximal sediment cores (Levy et al., 2016) and modeling studies (Gasson et al., 2016), suggest that during the middle Miocene the EAIS oscillated between states both larger and

33   smaller than present in response to fluctuations in CO_2 and temperature. After ~14 Ma, such proxy records suggest

34   general presence of the EAIS, but with potentially significant retreat during past warm periods, such as the mid-

35   Pliocene Warm Period (3.3–3.0 Ma) (e.g., Dutton et al., 2015 and references therein), when temperatures are thought

36   to have been 2–3°C warmer than preindustrial (Haywood et al., 2013) and CO_2 was ~400 ppm (Pagani et al., 2010;

37   Seki et al., 2010). Although valuable for elucidating long-term trends in sea-level change, these proxy records do not

38   directly record the volume of specific ice sheets. In contrast, glacial deposits from ice-free areas of Antarctica itself

39   provide direct geologic evidence for past ice sheet variability.

40   Previous geomorphic and glacial chronologic studies in the Transantarctic Mountains (TAM), a ~3000 km-long

41   topographic barrier through which outlet glaciers of the EAIS drain into the Ross Sea Embayment (Figure 1), suggest

42   the presence of pre-Pleistocene glacial deposits. Two distinct categories of deposits characterize the Antarctic glacial-

43   geologic record: basal tills of the Sirius Group (e.g., Mayewski, 1975; Mercer, 1972), which indicate at least one

44   period of temperate glaciation, and thin, bouldery drifts and moraines deposited by ice frozen to the bed (e.g., Prentice

45   et al., 1986), which overlie the older temperate deposits. In southern Victoria Land, Schaefer et al., (1999) reported a

46   minimum age of > 10 Ma for Sirius Group tills at Mt. Fleming. Similarly, relict subglacial flood deposits in the

47   Coombs Hills resulting from wet-based glaciation afford [3]He ages between ~8.5 and 10.5 Ma, assuming zero erosion,

48   and as much as ~15 Ma if erosion rates of 0.03–0.06 m/Ma are applied (Margerison et al., 2005). In the same region,

49   [40]Ar/[39]Ar ages on in situ ash layers interbedded with cold-based ablation tills in the Asgard Range date the transition

50   from temperate to polar glaciation to between 15 and 13.6 Ma (Sugden and Denton, 2004). The preservation of such

51   deposits over the last ~15 Ma has been invoked as evidence for persistent polar desert conditions, and by extension

52   the presence of the EAIS, since that time (Denton et al., 1993).

53   Chronologic constraints on the overlying cold-based deposits come primarily from surface-exposure dating, which

54   has been employed at several locations throughout the TAM, including southern Victoria Land (Brook et al., 1995,

55   1993; Brown et al., 1991; Bruno et al., 1997; Ivy-Ochs et al., 1995; Strasky et al., 2009); Beardmore (Ackert and Kurz,

56   2004) and Law (Kaplan et al., 2017) Glaciers in the central TAM; and Scott (Spector et al., 2017) and Reedy (Bromley

57   et al., 2010; Todd et al., 2010) Glaciers in the southern TAM. Approximately 30 previously published exposure ages

58   (see ICE-D:ANTARCTICA online archive: http://antarctica.ice-d.org) indicate the preservation of cold-based glacial

59   landforms in Antarctica that are at least 5 Ma in age. For example, a prominent boulder moraine in the Dominion

60   Range, upper Beardmore Glacier, was dated with [3]He to 5.2 Ma (Ackert and Kurz, 2004). Similarly, [10]Be ages from

61   erratic boulders at Reedy Glacier suggest deposition of the 'Reedy E drift' at > ~5 Ma (Bromley et al., 2010).
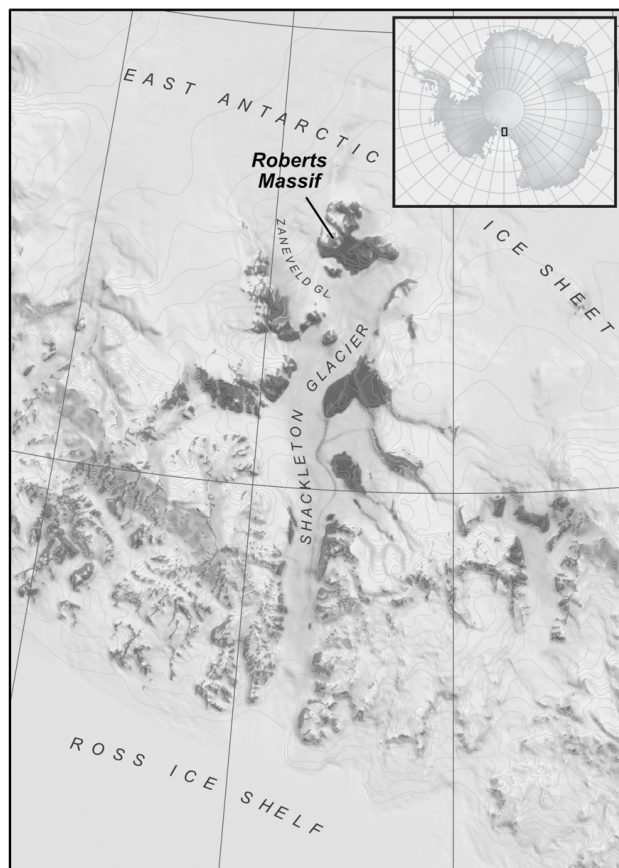
Figure 1. Location of Roberts Massif. The massif lies at the head of the Shackleton Glacier, which flows from the polar plateau of the East Antarctic Ice Sheet at ~2500 m elevation, down through the Transantarctic Mountains, to the Ross Ice Shelf near sea level. Basemap generated from the MODIS MOA (Scambos et al., 2007) and Antarctic Digital Database via the Quantarctica compilation (http://quantarctica.npolar.no).

62   To further constrain the pre-Pleistocene configurations of the EAIS, we exploit the extensive moraine record at Roberts
63   Massif, a high-elevation site in the central TAM, where studies on nearby nunataks have suggested that old (> 5 Ma)
64   deposits exist (e.g., Ackert and Kurz, 2004). Roberts Massif (86.374°S, 177.135°W) is a ~100 km² ice-free area
65   situated at the head of Shackleton Glacier, an outlet of the EAIS (Figure 1). The massif is bounded to the south and
66   east by the EAIS, to the north and west by the upper Shackleton Glacier, and to the northeast by an unnamed branch
67   of Zaneveld Glacier. Today, the EAIS at Roberts Massif is cold based and the environment is that of a polar desert.
68   We employed cosmogenic ^{3}He, ^{21}Ne, ^{10}Be, and ^{26}Al to date moraines at Roberts Massif to create a comprehensive
69   glacial-geologic record for this site comprising 180 samples. Our record affords an unprecedented view of EAIS
70   variability in the central TAM over the last ~15 Ma and provides valuable new insight into EAIS behavior during
71   periods of the Miocene and Pliocene, when temperatures and atmospheric CO_2 were likely similar to or higher than
72   today.

73   **2 Methods**

74   **2.1 Geomorphic Mapping and Sample Collection**

75   Fieldwork took place during the 2015–2016 and 2016–2017 austral summers. In the field, we identified and mapped

76   moraines, till deposits, and fault scarps on to 2 m-resolution satellite imagery provided by the Polar Geospatial Center,

77   University of Minnesota. We collected samples for surface-exposure dating from the upper surfaces of erratic boulders

78   located on moraine crests and drift sheets, focusing on boulders in stable positions (i.e., perched atop other boulders,

79   not broken) and exhibiting minimal evidence for surficial erosion. Owing to the prevalence of nuclide inheritance

80   documented by previous Antarctic cosmogenic studies (e.g., Stone et al., 2003; Todd et al., 2010), which is linked to

81   incomplete erosion by cold-based ice of previously exposed surfaces, we sampled large (generally > 1 m tall), angular

82   boulders, following the reasoning that such forms are (i) less likely to have been reworked from the underlying Sirius

83   Group tills than visibly molded, striated, and/or polished cobbles of exotic lithologies, and (ii) more likely to have at

84   least one side that is free of inherited nuclides.

85   We collected samples of ~1–5 cm thickness using either a hammer and chisel or drill and wedges. To characterize

86   each sampled boulder fully and document its geomorphic context, we described, measured, sketched, and

87   photographed each boulder from at least four different angles. We located samples in the field using an uncorrected

88   handheld GPS unit (estimated horizontal precision typically ± 6 m), and measured elevations by barometric traverse

89   from temporary benchmarks established using differentially corrected GPS and corrected to orthometric heights

90   relative to the EGM96 geoid. The estimated vertical precision of the temporary benchmarks is between ± 0.05 and ±

91   0.3 m. For barometric differential elevation measurements relative to the benchmarks, we used a Kestrel 4000

92   barometric altimeter and looped between samples and benchmarks to correct for time-dependent changes in

93   atmospheric pressure. The estimated total uncertainty in sample elevations measured using this procedure is ± 2.5 m,

94   reflecting the precision of the DGPS surveys and the barometer, and the reproducibility of differential barometric

95   elevation measurements of representative sites also surveyed by differential GPS in this and other studies. We

96   measured topographic shielding at sample sites using handheld compass and inclinometer and the procedure described

97   by Balco et al. (2008, with accompanying online material).

98   **2.2 Cosmogenic-nuclide measurements**

99   **2.2.1 Cosmogenic helium-3 analyses**

100   We measured cosmogenic ^{3}He concentrations in pyroxene separated from samples of Ferrar dolerite. To separate

101   pyroxenes at the University of Maine Cosmogenic Isotope Laboratory, we followed a modified version of the method

102   described by Bromley et al. (2014). We sieved crushed samples to isolate the 125–250 µm grain size fraction, which

103   was boiled for two hours in 10% HNO_3 to remove Fe oxides and other weathering products. We then removed lighter

104   minerals (mostly plagioclase) using a water-based heavy liquid with density 2.94 g/cm^3, and leached remaining

105   material in 5% HF to dissolve adhering plagioclase and remove outer surfaces of pyroxene grains potentially enriched

106   in implanted ^{4}He from U and Th decay (Blard and Farley, 2008; Bromley et al., 2014). Finally, etched pyroxenes were

107 passed through a magnetic separator and hand-picked to remove remaining contaminants under a binocular

108 microscope.

109 We then measured ^{3}He concentrations in clean pyroxene separates at the Berkeley Geochronology Center using the

110 BGC "Ohio" system, which consists of a MAP 215-50 sector field mass spectrometer with updated detectors and

111 counting electronics, coupled to a fully automated gas extraction and purification system. Gas extraction on this system

112 uses a laser "microfurnace" in which ~15-40 mg aliquots of pyroxene, encapsulated in Ta packets, are heated under

113 vacuum using a 150W, 810 nm diode laser coupled to a coaxial optical pyrometer in a feedback loop allowing control

114 of the pyrometer temperature. The pyrometer is calibrated by heating a thermocouple in an identical apparatus.

115 However, note that precise temperature measurement is not necessary for this work. In most cases (Table S2), we

116 extracted helium in an initial 15-minute heating step at 1225°C, followed by a second 15-minute heating step at

117 1325°C to ensure complete extraction. The second heating step typically contained 1–5% of total He released. We

118 added additional heating steps for a few representative samples to test for complete extraction, and found He signals

119 indistinguishable from blank. Gases released into the extraction line were purified by reaction with SAES getters and

120 frozen to activated charcoal at 12 K, after which helium was released into the mass spectrometer at 33 K. In all cases,

121 we measured ^{4}He signals on a Faraday cup and ^{3}He on a continuous dynode electron multiplier operated in pulse-
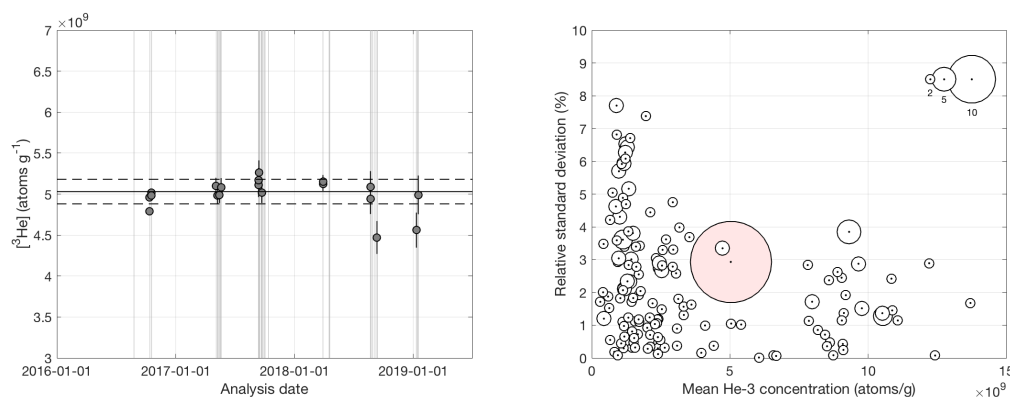
122 counting mode.

Figure 2. Quality-control data for ^{3}He measurements. Left panel, replicate analyses of CRONUS-P in all measurement periods during 2016-19. Light gray lines indicate dates samples in this study were analyzed. Error bars show 68% confidence estimates (e.g., 1 sigma); relatively large uncertainties and poor reproducibility in final two measurement periods reflect unusually nonlinear helium sensitivity and relatively large scatter in analyses of gas standards during these periods. Horizontal lines show mean and standard deviation of all measurements. Right panel, relative standard deviation of replicate analyses of 142 samples of Ferrar pyroxene analyzed during this study. 21 of these samples are not from Roberts Massif and therefore are not reported in this study but are included here for completeness. The size of the symbol indicates the number of times each sample was analyzed. The pink circle is CRONUS-P.

123 We quantified both ^{3}He and ^{4}He sensitivity by peak height comparison between samples and aliquots of custom-mixed

124 helium gas standards, calibrated using direct pressure measurements of both isotopes using Baratron capacitance

125 manometers, containing between 1.57 x 10^{-18} and 4.71 x 10^{-16} moles of ^{3}He and between 4.39 x 10^{-14} and 1.26 x 10^{-11}

126   moles of ^{4}He. Ferrar pyroxene has relatively high and highly variable ^{4}He concentrations, and the MAP 215 mass

127   spectrometer displays a significant pressure dependence on He sensitivity (Burnard and Farley, 2000), so accurately

128   quantifying machine sensitivity over a wide pressure range was an important aspect of this work. We addressed this

129   by (i) source tuning at He pressures similar to those expected for sample analyses to improve linearity in the pressure

130   range of interest, and (ii) ensuring that observed He pressures in sample analyses were bracketed within the pressure

131   range available from standard analyses. In many cases, this required discarding results of an initial analysis and

132   reanalyzing the sample with a different size aliquot calculated to match sample and standard pressures. Total process

133   blanks measured on empty Ta packets had less than 10^5 atoms ^{3}He and 10^{10} atoms ^{4}He, which is negligible for all

134   samples discussed here. Reported measurement uncertainties in ^{3}He concentrations include uncertainties from ^{3}He

135   counting statistics (typically 1–2%) as well as the variance in sensitivity inferred from gas standard analyses spanning

136   the pressure range of interest (typically 1–3%).

137   As additional quality control measures, we analyzed aliquots of the CRONUS-P pyroxene standard (Blard et al., 2015)

138   together with samples throughout each period of analysis, and made replicate analyses of a total of 121 pyroxene

139   samples as well as an additional 21 samples of Ferrar pyroxene from other Antarctic sites (Figure 2). In each of 6

140   distinct measurement periods between 2016-2019, we analyzed 2-4 aliquots of CRONUS-P. Although average

141   measured ^{3}He concentrations in individual measurement periods varied from 4.80 ± 0.30 x 10^9 atoms/g to 5.14 ± 0.1

142   x 10^9 atoms/g, data from different measurement periods were not distinguishable as separate populations. The mean

143   and standard deviation of 19 measurements during the entire period was 5.03 ± 0.15 x 10^9 atoms/g (2.9%), which is

144   indistinguishable from the accepted value of 5.02 x 10^9 (Blard et al., 2015). Replicate analyses of other samples had

145   a mean relative standard deviation of 2.2% (Figure 2). As expected from counting statistics, replicate scatter varied

146   with ^{3}He concentrations, ranging from 3% for concentrations < 2 x 10^9 atoms/g to 1.5% for concentrations > 7 x 10^9

147   atoms/g.

148   Ferrar pyroxene is known to contain a non-zero concentration of non-cosmogenic (presumably magmatic) ^{3}He. Kaplan

149   et al. (2017), Margerison et al. (2005), and Ackert (2000) obtained maximum limiting concentrations for non-

150   cosmogenic ^{3}He of 5-–7 x 10^6 atoms/g, which are consistent with an unpublished estimate (Balco, unpublished data)

151   of 3.3 ± 1.0 x 10^6 atoms/g. As this is 1.2% of the lowest total ^{3}He concentration measured in a Roberts Massif erratic

152   in this study, and 0.1 % of the average concentration observed, we disregard it and assume that all observed ^{3}He in

153   pyroxene is cosmogenic.

154   **2.2.2 Cosmogenic beryllium-10 and aluminum-26 analyses**

155   We purified quartz from sandstone samples using established physical and chemical procedures (e.g., Schaefer et al.,

156   2009) at the University of Maine Cosmogenic Isotope Laboratory. Chemical extraction of beryllium and aluminum

157   and preparation of BeO and Al_2O_3 targets took place at the University of Maine and Lawrence Livermore National

158   Laboratory (LLNL). Ratios of ^{10}Be/^{9}Be were measured relative to the 07KNSTD standard (Nishiizumi et al., 2007) at

159   LLNL and corrected for background ^{10}Be by procedural blanks with a range of 23,000–44,000 atoms. Al isotope ratios

160   are measured relative to the KNSTD standardization of (Nishiizumi, 2004), and corrected for a procedural blank of

161   75,000 ± 75,000 atoms. Note that blank corrections for both [10]Be and [26]Al are negligible for samples in this study.

162   One measurement of the CRONUS-A quartz standard (Jull et al., 2015) run together with these samples yielded 3.491

163   ± 0.047 x 10^7 atoms/g [10]Be and 1.494 ± 0.030 x 10^8 atoms/g [26]Al (Table S5), indistinguishable from accepted values

164   for both nuclides. Reported uncertainties for [10]Be and [26]Al measurements include uncertainties in AMS isotope ratio

165   measurement, process blanks, and [9]Be/[27]Al concentrations.

2.2.3 Cosmogenic neon-21 analyses

167   We measured [21]Ne in the same quartz separates used for [10]Be analysis using the BGC "Ohio" noble gas mass

168   spectrometer system also used for [3]He measurements and described above. Aliquots of quartz samples were degassed

169   in two heating steps at 850° and 1100°C, and calculations of excess [21]Ne (see below) are based on total Ne released

170   in both heating steps. Ne isotope measurements at BGC use a [39]Ar spike to quantify and correct for the [40]Ar^{++}

171   interference on mass 20, and are described in Balco and Shuster (2009). We quantified Ne abundances by peak height

172   comparison between samples and aliquots of an air standard containing between 5 x 10^{-16} and 2 x 10^{-14} mol Ne and

173   calibrated using a Baratron capacitance manometer. In contrast to helium, neon sensitivity was linear within this range

174   at all times. Corrections for mass discrimination, when necessary, are also based on the air standard and assumed

175   atmospheric [21]Ne/[20]Ne and [22]Ne/[20]Ne ratios of 0.002959 and 0.1020, respectively. A total of 20 analyses of the

176   CRONUS-A quartz standard during the period of this study yielded mean and standard deviation of 319.8 ± 6.3

177   Matoms/g (2% RSD) excess [21]Ne, indistinguishable from the accepted value of 320 Matoms/g (Vermeesch et al.,

178   2015).

179   Neon isotope ratios, as observed in previous studies for TAM sandstones, were indistinguishable from the

180   atmospheric-cosmogenic mixing line (see supplementary Table S3). However, Balco et al. (2019) and Middleton et

181   al. (2012) have also shown that significant concentrations of nucleogenic [21]Ne produced by decay of trace U and Th

182   are present in quartz from this lithology. To calculate cosmogenic [21]Ne concentrations in quartz samples, therefore,

183   we first calculated excess [21]Ne with respect to atmospheric composition, followed Balco et al. (2019) in assuming that

184   excess [21]Ne consists of both cosmogenic and nucleogenic [21]Ne, and estimated nucleogenic [21]Ne concentrations using

185   the following procedure. First, we measured excess [21]Ne concentrations in a set of six sandstone samples from ice-

186   proximal sites at upper Roberts Massif that have apparent [10]Be exposure ages less than 10 ka, and one additional

187   sample with an apparent [10]Be exposure age of 75 ka. Assuming that these samples have experienced a single period

188   of exposure, we calculated the [21]Ne concentration attributable to this exposure and subtracted it from total excess [21]Ne

189   concentrations to obtain estimates of nucleogenic [21]Ne; resulting mean and standard deviation for nucleogenic [21]Ne

190   estimates in these samples are 10.5 ± 2.8 Matoms/g, similar to but slightly higher than estimates for Beacon Group

191   sandstones in the Dry Valleys region (Balco et al., 2019; Middleton et al. 2012). We then measured U and Th

192   concentrations in quartz and computed apparent (U-Th)/[21]Ne closure ages as described in Balco et al. (2019);

193   excluding one outlier attributed to a spurious Th measurement, the mean and standard deviation of apparent closure

194   ages is 603 ± 110 Ma. If we assume that all other sandstone erratics from Roberts Massif that we analyzed in this

195   study have a similar source and therefore a similar apparent closure age, we can estimate nucleogenic [21]Ne

196   concentrations using U and Th concentrations and this closure age estimate. Note that this apparent closure age is

197   older than the depositional age of the Beacon Group. If these sandstone samples are derived from the Beacon group,

198   therefore, it is most likely inaccurate as a cooling age. However, the provenance of the sandstone erratics is unknown,

199   and in any case this inaccuracy would not affect the assumption that Roberts Massif sandstone erratics have a single

200   characteristic apparent closure age. Table S4 shows the results of this procedure. For samples with less than 200

201   Matoms/g total excess ^{21}Ne, we measured U and Th concentrations in individual samples and applied the mean closure

202   age inferred from the ice-proximal samples, which resulted in subtraction of up to 20% of total excess ^{21}Ne as

203   nucleogenic and had a significant effect on results. For samples with higher ^{21}Ne concentrations, the uncertainty in

204   the nucleogenic ^{21}Ne estimate is negligible and we used an average value rather than measuring U and Th in individual

205   samples. For example, for samples from the Southwest Col on Misery Platform, discussed below, estimated

206   nucleogenic ^{21}Ne is less than 0.5% of total excess ^{21}Ne. Reported uncertainties for ^{21}Ne measurements, as for ^{3}He, are

207   derived from counting statistics as well as reproducibility of the gas standards.

2.2.4 Treatment of replicates for cosmogenic noble gas measurements

209   For the majority of samples, we made replicate ^{3}He and ^{21}Ne measurements and performed chi-squared tests on

210   replicate sets with the null hypothesis that all measurements on the same sample belong to a single population and

211   disagree only because of measurement uncertainty. If we could not reject the null hypothesis at 95% confidence, we

212   took the error-weighted mean of replicate analyses as the true nuclide concentration and the standard error as the

213   uncertainty. If the null hypothesis was rejected, we used the arithmetic mean and standard deviation. A caveat to this

214   procedure, however, is that we found that our ^{3}He results from CRONUS-P during the period of this study did not

215   pass a chi-squared test (p = 0.02), indicating that our internal uncertainty estimates for individual ^{3}He measurements

216   are underestimating the true scatter in multiple measurements of the same sample. Thus, we adjusted calculated

217   uncertainties upward when necessary such that no ^{3}He concentration has a relative uncertainty less than 2.9%, the

218   relative standard deviation of CRONUS-P measurements. ^{21}Ne results from CRONUS-A, on the other hand, passed

219   the chi-squared test (p = 0.35), so we did not make a similar adjustment to ^{21}Ne data. However, cosmogenic ^{21}Ne

220   concentrations do include an additional uncertainty derived from nucleogenic ^{21}Ne subtraction after averaging of

221   replicates.

2.3 Surface exposure age calculations

223   We calculated exposure ages from measured nuclide concentrations using Version 3 of the online exposure age

224   calculator described by Balco et al. (2008) and subsequently updated (http://hess.ess.washington.edu). We employed

225   the time-dependent "LSDn" scaling method of Lifton et al. (2014) and the Antarctic atmosphere model of Stone

226   (2000). Production rate calibration for ^{10}Be, ^{26}Al, and ^{3}He use the "primary" calibration data sets of Borchers et al.

227   (2016) for these nuclides, and we compute ^{21}Ne production rates by assuming a $^{21}Ne/^{10}Be$ production ratio of 4.03

228   (Balco et al., 2019; Balco and Shuster, 2009b; Kober et al., 2011). In contrast to exposure-dating studies that are

229   located at similar altitude and latitude to production rate calibration sites, our study involves significant extrapolations

230   from the locations of calibration data, mostly at low elevation and high latitude or high elevation and low latitude, to

231   the high-elevation-high-latitude sites at Roberts Massif. Scaling methods that can be fit equivalently to the calibration

232 data predict different production rates at our sites. Specifically, production rates predicted by LSDn scaling are ~15%

233 higher than those predicted by the scaling method of Lal (1991) and Stone (2000) (the 'St' and 'Lm' scaling methods

234 of Balco et al., 2008). However, at several high-elevation sites in Antarctica, including Roberts Massif, measured [10]Be

235 and [26]Al concentrations are significantly higher than values for production-decay saturation predicted by the St and

236 Lm methods, indicating that these methods overpredict production rates at high-elevation-high-latitude locations (see

237 discussion in https://cosmognosis.wordpress.com/2016/09/09/ saturated-surfaces-in-antarctica/). On the other hand,

238 saturation concentrations predicted by the LSDn method are consistent with the highest measured [10]Be and [26]Al

239 concentrations in Antarctica. Thus, we conclude that, at least in the high TAM, exposure ages calculated using LSDn

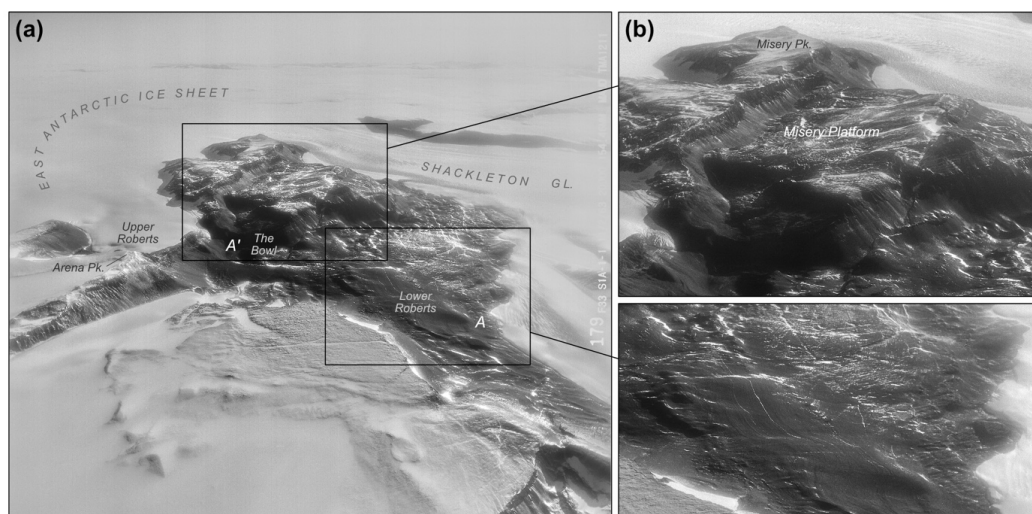240 scaling are likely accurate, and exposure ages calculated using St/Lm scaling would be spuriously old.

Figure 3. Oblique aerial photograph of Roberts Massif looking west along the spine of the Transantarctic Mountains, with the East Antarctic Ice Sheet to the left. Enlargement (A) shows Misery Platform, which is the hanging wall of the large normal fault that bisects the massif. (B) shows the extensive moraine sequence at lower Roberts Massif. The moraine sequence at Upper Roberts (Fig. 7) faces west and is hidden from this viewing angle. A and A' match Figure 4. Image is 1963 U.S. Navy trimetrogon aerial photograph, TMA 1211/179 R.

241 Additional uncertainties in exposure-age estimates derive from the choice of production rate calibration data.

242 Estimated total uncertainties for [10]Be exposure ages derived from calibration data are ~6% (Borchers et al., 2016).

243 Yet, any [10]Be calibration dataset that predicted significantly lower production rates, and therefore lower saturation

244 concentrations, would not be consistent with the [10]Be data from the Southwest Col (see discussion in section 4.3).

245 These data permit that we have underestimated [10]Be production rates, but not that we have overestimated them.

246 However, the majority of data in this study are [3]He exposure ages, and we have no similar constraint on [3]He production

247 rates. [3]He production rate calibration data display substantially more scatter than [10]Be, and estimates on total global

248 uncertainty for [3]He exposure dating range from less than 2% (Goehring et al., 2018) to more than 10% (Borchers et

249 al., 2016; Phillips et al., 2016). Production rate calibration uncertainty therefore may be significant for [3]He results.

3 Results

3.1 Field Observations

Roberts Massif is defined topographically by large-scale normal faulting that has produced escarpments as much as ~1200 m in relief (Figure 3). These faults delineate a number of broad, sub-horizontal surfaces, including a lower-elevation platform (hereafter 'Lower Roberts'), a middle-elevation platform, comprising the Misery Platform and Upper Roberts sites, and the high peaks of the massif, including Misery Peak (2725 m) and Arena Peak (informal name; 2700 m). Local bedrock comprises sandstones of the Beacon Supergroup and pyroxene-bearing Ferrar dolerite, which includes a fine-grained variety and a friable, coarse-grained variety. Notably, the termini of the EAIS, Shackleton Glacier, and the unnamed spur of Zaneveld Glacier at Roberts Massif are relatively free of debris, containing only the occasional boulder. Further, we did not observe any evidence of glacial outwash or liquid water at any of these margins, indicating that the ice bounding Roberts Massif is currently cold-based.

3.1.1 Lower Roberts

In the southern portion of the Lower Roberts area, a complex of faults forms a deep, back-tilted basin named "The Bowl" by Hambrey et al. (2003). With the exception of a 100 m-relief bedrock hill, referred to here as the Central Rise, and the Bowl, the Lower Roberts area exhibits relatively gentle topography (Figure 4). Dolerite bedrock surfaces outcrop at several locations throughout Roberts Massif, and commonly exhibit glacial polish, striations, and molding consistent with erosion beneath a wet-based glacier. Most of these bedrock outcrops are directly overlain by semi-lithified, poorly sorted pockets of sediment (several meters thick in places), containing deeply striated gravel- to cobble-sized clasts of heterogenous, non-native lithologies embedded in an olive-gray, clay-rich matrix (Figures 4 and 5). We interpret these sediments as lodgement tills associated with the Sirius Group. First described by Mercer (1972), the Sirius Group occurs throughout the upper (> ~2000 m elevation) TAM as erosional remnants of clay-rich diamicton that are correlated with at least one period of past temperate glaciation. An in-depth sedimentological study of glacially eroded bedrock surfaces and Sirius Group tills at Roberts Massif, and other locations along upper Shackleton Glacier, is provided by Hambrey et al. (2003).

Bedrock and Sirius Group tills are blanketed by patchy glacial drift, comprising primarily angular, cobble-to-boulder-sized clasts with little-to-no fine-grained material (Figure 5). Ferrar dolerite is the most abundant lithology, although this drift includes the occasional sandstone boulder, as well as rounded cobbles reworked from the underlying tills described above. A key feature of this drift deposit is the abundance of open-work boulder moraines, which we targeted for surface-exposure dating (Figure 6). These low relief (1–2 m high) ridges are composed primarily of large, angular dolerite boulders and are oriented sub-parallel to the modern ice edge, marking former marginal positions of the EAIS to the South and the unnamed spur of the Zaneveld glacier to the north. The sediments of these drifts and associated boulder-belt moraines exhibit characteristics typical of cold-based glaciation, being thin, patchy, and clast-supported with little-to-no fine grained material (Figures 5 and 6) (Atkins, 2013). Furthermore, clasts are generally angular and lack the striations, polish, and molding associated with erosive wet-based ice.
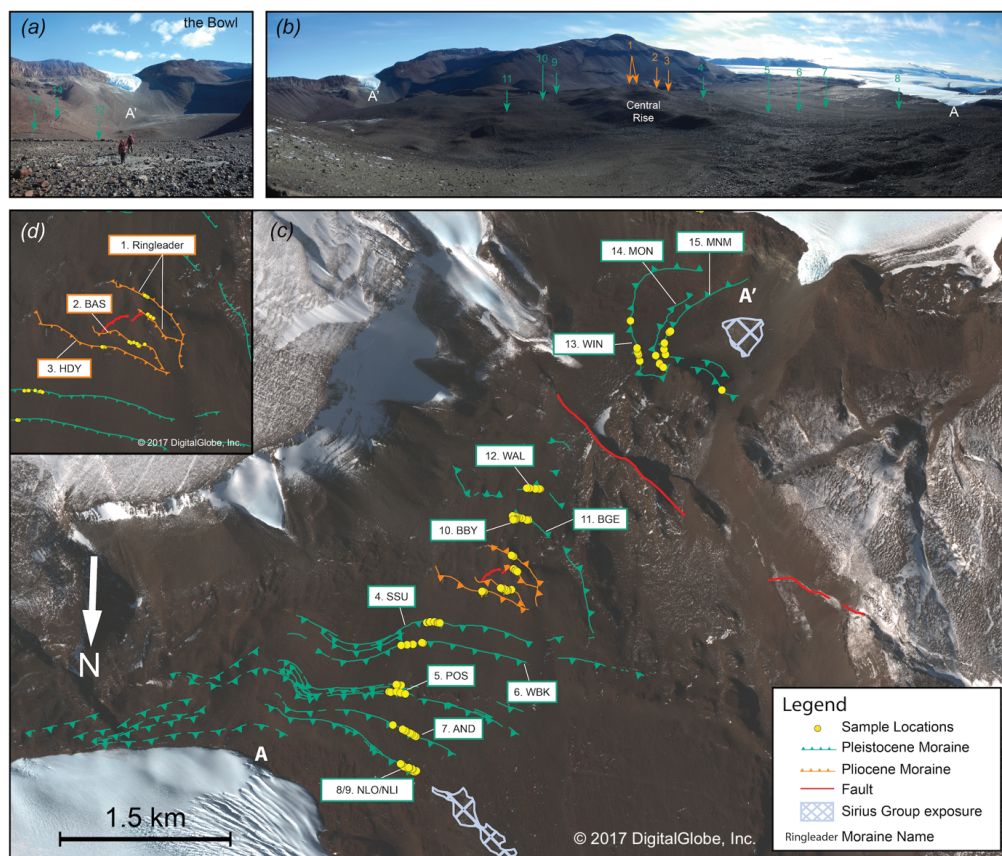
Figure 4: Map of Lower Roberts. a) Photograph of the Bowl, showing cold-based drift and moraines overlying Sirius Group deposits, which appear light gray, and b) photo of the Lower Roberts area shown with arrows pointed to sampled moraines, with numbers corresponding to moraine names in (c) and letters A and A' corresponding to positions in (c). c) Glacial geomorphic map showing moraines and sample locations at Lower Roberts, as well as the location of observed Sirius Group outcrops. The basemap is derived from Worldview-2 satellite imagery (copyright 2017, DigitalGlobe, Inc.).

284   We identified and sampled for surface-exposure dating 15 moraines throughout the Lower Roberts area. We focused

285   on the most prominent, laterally continuous moraines, which comprise accumulations of stacked boulders, and avoided

286   the numerous discontinuous moraine mounds and isolated erratic boulders, from which former ice marginal positions

287   are difficult to reconstruct. The stratigraphically oldest moraine in the Lower Roberts sequence, the Ringleader

288   moraine (informal name) encircles the summit of the Central Rise, indicating that north- and south-flowing ice masses

289   once converged to form a continuous ice surface across the Lower Roberts area at least ~170 m higher than the modern

290   ice margin to the north. From the Ringleader moraine, at the highest position in the Lower Roberts site, we sampled

291   northern (extending from Ringleader to A in Figure 4) and southern (extending from Ringleader to A' in Figure 4)

292   moraine transects. Listed in stratigraphic order, the northern transect included the BAS, HDY, SSU, WBK, POS,

293   AND, and NLO/NLI moraines (moraine initials correspond to informal names and sample ID suffixes listed in the

294   ICE-D Antarctica online database and Table S1); from the southern transect we sampled the BBY, BGE, WAL, WIN,

295   MON, and MNM moraines. Notably, the POS moraines constitute a complex of three main ridges, while the NLO/NLI

296   moraines comprise two distinct ridges spaced only by ~5 m.

297   The youngest deposit at Roberts Massif comprises a thin layer of sandstone and dolerite debris that extends several

298   tens of meters beyond the current ice margins. Clasts are relatively unweathered (i.e., exhibit minimal staining and/or

299   exfoliation), and exhibit fresh scuff marks [abrasions formed as cold-based ice drags entrained boulders across

300   underlying surfaces (Atkins et al., 2002)] (Figure 5f). With the exception of a few discontinuous segments, this unit

301   generally is not associated with distinct moraines. Based on strong similarities in position, morphology, and relative

302   weathering with deposits reported from other TAM sites (e.g., Todd et al., 2010), we correlate the youngest drift unit

303   at Roberts Massif with the most recent Late Quaternary expansion of Shackleton Glacier/EAIS and do not discuss it

304   further.

305   Outboard of this relatively unweathered limit, drift and moraine boulders become progressively more weathered with

306   distance from and elevation above the modern ice. For instance, dolerite boulders belonging to the outermost deposits

307   of the HDY, BAS, and Ringleader moraines (up to 3 km from and 170 m above the modern ice margin) exhibit dark

308   red staining, pitting of up to ~0.5 cm depth, exfoliation up to ~4 mm, and weathering rinds 1–2 mm thick, while the

309   presence of sandstone clasts is increasingly rare (Figure 6d). In contrast, dolerite boulders that we sampled on the

310   innermost moraines were generally blue-grey in color and lacked significant weathering characteristics, such as

311   staining or pitting (Figure 6c). Although the boulders on the outermost moraines at Roberts Massif display more

312   pronounced weathering than those on the inner moraines, the characteristics described here represent relatively

313   minimal surface weathering compared to slightly warmer and wetter Antarctic locations, such as the McMurdo Dry

314   Valleys. There, ~3 Ma clasts, which are similar in age to those on the HDY, BAS, and Ringleader moraines (Section

315   3.4), display pitting greater than 4 cm depth (Swanger et al., 2011). Additionally, we did not observe any cross-cutting

316   relationships between moraine crests throughout Lower Roberts, either on the ground or in satellite imagery.

317   Therefore, we conclude that moraines at this site increase in age with distance away from and elevation above the

318   modern ice sheet surface. Altogether, these surface-most deposits indicate that the Lower Roberts area records > 15

319   prior expansions of cold-based ice.

Figure 5: Views of drifts and tills described at Roberts Massif. a) The gray, fine-grained Sirius Group deposits atop striated dolerite bedrock; b) Sirius Group exposed in section in the Bowl; c) Striated, glacially molded Sirius cobble embedded in a fine-grained matrix; d) Sample 16-ROB-089-COL, a freshly-scoured sandstone clast in the Bowl, likely deposited as a thin drift sheet atop older deposits during a Late Quaternary expansion of the EAIS; e) cold-based AND moraine, which is Pleistocene in age; and f) Misery B moraine, which is Miocene in age.

Figure 6: Photographs of moraines and sampled boulders at Roberts Massif. a) Blue-gray dolerite boulder 16-ROB-010-NLO on the second moraine from the modern EAIS in the Lower Roberts northern transect; b) Red-stained dolerite boulder 16-ROB-059-RIN on the Ringleader moraine, the outermost moraine in the Lower Roberts area; c) Relatively unweathered sandstone boulder 16-ROB-009-NLO; d) Red-stained/varnished sandstone boulder 16-ROB-062-RIN on the Ringleader moraine; e) Relatively unweathered, blue-gray dolerite boulder 15-ROB-064-MUS on the Musik moraine, the innermost moraine at Upper Roberts; and f) Weathered/red-stained dolerite boulder 15-ROB-038-ARM on the Arena moraine, the outermost moraine at Upper Roberts.

3.1.2 Upper Roberts

The Upper Roberts site is situated on a steep, west-facing slope of Arena Peak, directly adjacent to the northward flowing lobe of the EAIS that ultimately flows over the Bowl headwall (Figure 7). Here, we mapped glacial drift and moraines identical in character to those at Lower Roberts, indicating deposition by a cold-based EAIS. Similar to observations at Lower Roberts, a fresh-looking drift of sandstone and dolerite boulders extends several tens of meters beyond the modern ice edge. At the Upper Roberts site, that fresh deposit is associated with a low-relief (~1.5 m) ridge. We attribute this deposit to the most recent expansion of the EAIS during the Late Quaternary and do not discuss it further in this paper. We focused on five moraine ridges located along a vertical transect between ~60 m and 150 m above and oriented sub-parallel to the modern ice surface (2150 m). In order of descending elevation, we identified and sampled the Arena (2300 m), Eine (2260 m), Kleine (2240 m), Nacht (2220 m), and Musik (2220 m) moraines (informal names). Additionally, we mapped moraine segments preserved both within and above (up to ~2500 m elevation) this transect, but, owing to lateral discontinuity and poor preservation on high-gradient slopes, we did not sample these limits for surface-exposure dating. As at Lower Roberts, the general increase in boulder-surface weathering and the absence of cross-cutting moraine stratigraphy (determined from field observations and satellite imagery) suggests that glacial deposits at Upper Roberts become older with increasing elevation above the modern EAIS (Figure 6).

3.1.3 Misery Platform

Misery Platform is a broad, gently sloping platform in the southwest part of Roberts Massif (Figures 3 and 8). Comprising the top surface of the hanging-wall block of a large normal fault, Misery Platform is bounded to the south by a ~300–340 m-high fault scarp. At the base of the scarp, we mapped a series of arcuate moraine ridges (here termed the Misery moraines), four of which we sampled for exposure-age dating (Figures 8, 9). The southern edge of the footwall block, which includes Misery Peak (2723 m elevation), drops steeply to the EAIS surface at ~2200 m elevation, and exhibits south-facing, amphitheater-shaped valleys that are occupied partially by north-flowing lobes of the EAIS (Figure 8). The largest of these valleys is located directly south of the Misery Moraines, and its extension above the current surface of the EAIS suggests that this lobe of ice was significantly thicker in the past. Further, a thin drift of glacial erratics atop the footwall block at ~2550 m elevation mark where a north-flowing lobe of the EAIS overtopped the broad slopes east of Misery Peak and cascaded down the escarpment, where it deposited the Misery moraines on the platform below. This interpretation requires that the Misery moraines (a) postdate the formation of the fault scarp and (b) were deposited by an EAIS that was sufficiently thick (> 300 m above the current surface) to overtop the footwall block. Although the Misery moraines are similar in elevation to those sampled at Upper Roberts, they represent the highest former ice surface elevation of the EAIS examined in this study.
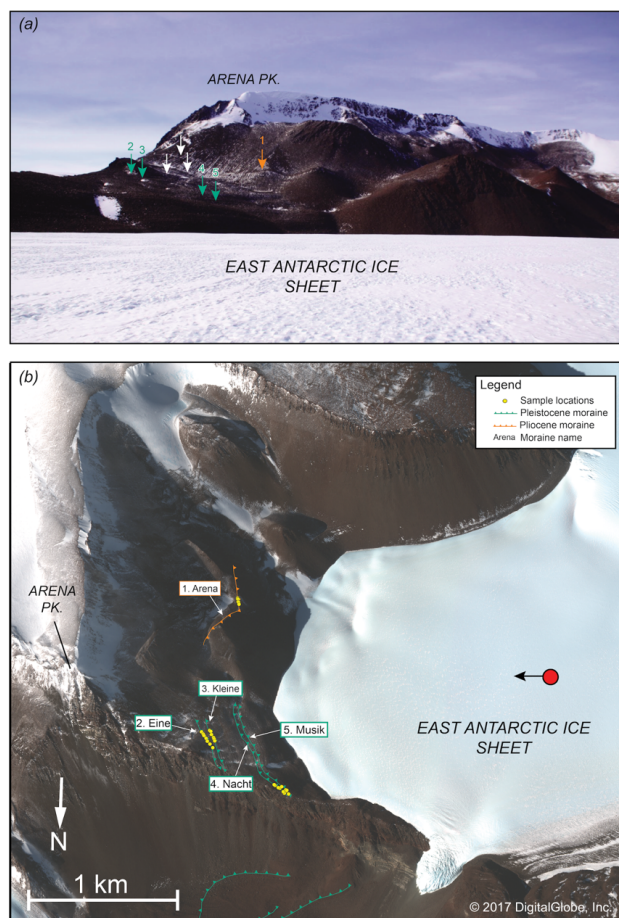
Figure 7. Upper Roberts Massif. a) Photograph of the Upper Roberts transect with moraines marked by arrows, numbered corresponding to sampled moraines in (b). White arrows in (a) denote undated moraines. b) Geomorphic map of Upper Roberts. The red circle and arrow shows the location and vantage of photo in (a). The basemap in (b) is derived from Worldview-2 satellite imagery (copyright 2017, DigitalGlobe, Inc.).

351 Compared to moraines at Lower and Upper Roberts, the Misery moraines are relatively broad and high-relief (~2–5
352 m high) and comprise finer matrix material (silt-to-gravel). Moraine crests are mantled with angular dolerite boulders
353 exhibiting pronounced weathering features, including deep red-to-purple staining, 2–3 mm-thick weathering rinds,
354 and ventifaction pits of up to 2 cm depth. On the basis of these physical characteristics, they appear older than the
355 outermost moraines at both Lower and Upper Roberts. Therefore, we interpret the Misery moraines as cold-based ice-
356 marginal features marking the ostensibly oldest and most extensive EAIS terminus positions that we documented at
357 Roberts Massif. We used cross-cutting relationships of the Misery moraines to determine their stratigraphic order.
358 From outermost (oldest) to innermost (youngest), we sampled boulders on the following moraine crests: Misery D,
359 Misery A, Misery B, Misery C (note that the designations A-D are field designations reflecting the sequence of sample
360 collection, not the stratigraphic order; Figure 8). Importantly, we avoided sampling adjacent to overlapping moraine
361 segments.

16

362   Immediately outside of, and stratigraphically underlying, the Misery moraines, the weathered bedrock surface is
363   mantled with a thin patchy ablation till, dominated by dolerite boulders and a small number of sandstone clasts, and
364   associated with a coarse-grained sand and gravel deflation surface. We observed this unit throughout Misery Platform
365   and collected samples for surface-exposure dating from boulders on Southwest Col, located approximately 1.5 km
366   northwest of the Misery moraine complex and 400 m above the modern surface of Shackleton Glacier (Figure 8).
367   Here, the ablation till ('Southwest Col drift') mantles a bedrock surface of heavily stained and deeply exfoliated
368   coarse-grained dolerite. In places, granular sediments fill joints and depressions in the bedrock. These sediments are
369   characterized by red-stained silt-to-gravel-sized grains, which may derive from the disintegration of the dolerite
370   bedrock, and gravel-to-cobble-sized clasts of various lithologies. In contrast to the Sirius Group deposits observed
371   elsewhere at Roberts Massif, boulders comprising Southwest Col drift are predominantly dolerite (as opposed to a
372   broad mix) and generally more angular.

373   We sampled three dolerite clasts (1 boulder and 2 cobbles) and four sandstone clasts (3 boulders and 1 cobble), all of
374   which are perched on bedrock and/or interstitial sediments, for surface-exposure dating. The surface of the dolerite
375   boulder (15-ROB-28-COL) exhibits deep red staining and evidence of significant wind abrasion, except on the lee
376   side where there is a thick red-brown weathering rind (Figure 9). The sandstone boulders (15-ROB-32-COL, 15-ROB-
377   33-COL, and 15-ROB-34-COL) exhibit orange-to-red staining, surface varnish, and ventifaction of up to 4 cm depth.
378   Based on the thin nature of this deposit, we interpret the Southwest Col drift as a cold-based ablation till deposited by
379   the EAIS. Owing to its weathering state, we suggest that this deposit is the oldest glacial unit in our record. Surface-
380   exposure ages from this site therefore provide a minimum-limiting age for temperate glaciation at Roberts Massif.

381   **3.1.4 Summary of Field Observations**

382   We mapped three primary surfaces at Roberts Massif (listed in stratigraphic order): glacially molded and striated
383   dolerite bedrock, temperate-style tills belonging to the Sirius Group, and cold-based drifts associated with openwork
384   boulder moraines. All samples collected for surface-exposure dating are derived from the cold-based deposits marking
385   former positions of the EAIS. At both the Lower and Upper Roberts sites, weathering patterns and the lack of cross-
386   cutting moraines suggest that relative moraine ages increase with distance from, and elevation above, the modern ice
387   sheet margin. Deposits on Misery Platform (the Misery moraines and the Southwest Col drift) exhibit more advanced
388   subaerial weathering than our other sites, indicating that these deposits are significantly older. In Section 4.2, we
389   describe results from cosmogenic-nuclide measurements made on samples from 23 separate moraine ridges and one
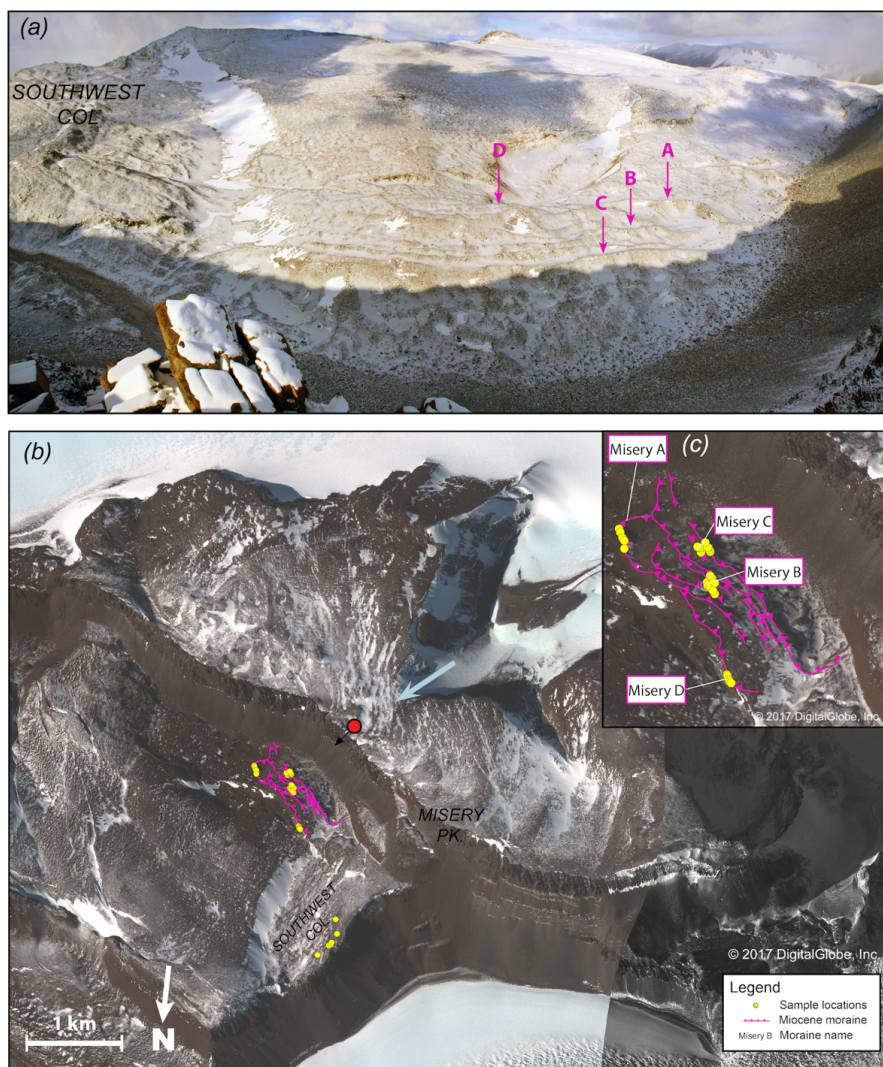390   drift sheet.

Figure 8: Map of Misery Platform. a) Photo of the Misery Moraines. Pink arrows point to the sampled Misery Moraines and are labelled with the corresponding moraine letter. The location of the Southwest Col drift is also labeled. The photo was taken from the location of the red circle in (b) looking in the direction of the black arrow (vantage to the northeast). b) Geomorphic map of the Southwest Col area. The Southwest Col Drift mantles the bedrock outboard of the Misery moraines. The blue arrow denotes the direction of ice flow when the Misery Moraines were deposited. The basemap in (b) and (c) is derived from Worldview-2 satellite imagery (copyright 2017, DigitalGlobe, Inc.).

Figure 9: Photographs of boulders from the Misery Platform. a) Dolerite boulder 15-ROB-017-MZC on the Misery C moraine; b) Dolerite boulder 15-ROB-028-COL at the Southwest Col; c) Sandstone boulder 15-ROB-035-COL at the Southwest Col; d) Sandstone cobble 15-ROB-029-COL at the Southwest Col.

3.2 Results from Cosmogenic-Nuclide Measurements

We made cosmogenic ^{3}He measurements in pyroxene from 167 dolerite boulders; 38 ^{21}Ne and 13 ^{10}Be measurements in quartz from 13 sandstone boulders; and two ^{26}Al measurements in quartz from two sandstone boulders (also measured for ^{21}Ne and ^{10}Be). Samples were derived from 23 distinct moraine crests and one glacial drift sheet (Southwest Col). Apparent exposure ages span two periods: ~13–8 Ma at Misery Platform and ~3 Ma–400 ka at Upper and Lower Roberts (Tables 1 and S1). "Apparent" exposure ages refer to the calculated age of the boulder given the measured nuclide inventory, assuming that the boulder has experienced only one period of exposure, with no erosion or burial during that time. Boulder information, nuclide concentrations, complete step-degassing results for ^{3}He and ^{21}Ne are summarized in Tables S2, S3, and S5, and the full dataset is archived online in the ICE-D:ANTARCTICA database (http://antarctica.ice-d.org). In this section, we summarize these cosmogenic-nuclide data and highlight the

19

401   possible effects of surface erosion and other geomorphic processes on exposure ages, which ultimately lead us to

402   estimates of the emplacement age of the moraines.

3.2.2 Constraints on erosion rates from paired ^{10}Be-^{21}Ne measurements

404   As the majority of landforms at Roberts Massif are several million years old, quantifying the magnitude of surface

405   erosion is key to accurate exposure-dating. Here, we summarize geochemical data and field observations that allow

406   us to place limits on long-term erosion rates. Four sandstone erratics at Southwest Col have ^{10}Be concentrations close

407   to predicted production-erosion saturation values, and apparent ^{21}Ne exposure ages of 9–12 Ma. As these samples

408   have nearly the highest concentrations of these nuclides yet measured on Earth, concentration measurements are

409   correspondingly (and unusually) precise, making it possible to use the paired ^{10}Be/^{21}Ne data to simultaneously infer

410   exposure ages and surface erosion rates from these samples (Figure 10) (Gillespie and Bierman, 1995; Lal, 1991).

411   Given the assumption that these samples have experienced continuous exposure at a steady erosion rate, the ^{10}Be/^{21}Ne

412   data imply true exposure ages in the range 12–15 Ma, but varying surface erosion rates in the range 0.5–3 cm/Myr.

413   These low erosion rates are consistent with our field observations pertaining to surface erosion of these sandstones as

414   described in Section 3.1.3.

415   Apparent ^{3}He exposure ages from three dolerite clasts also located on Southwest Col, and which therefore should have

416   the same true exposure age as the sandstone clasts, are 8.6 Ma, 10 Ma, and 11 Ma. Assuming that the true exposure

417   age of the deposit is no greater than 14.5 Ma, as implied by the two-nuclide data for the highest-nuclide-concentration

418   sandstone (15-ROB-032-COL) shown in Figure 10, this implies maximum erosion rates for the dolerite clasts of 3.8,

419   2.7, and 1.9 cm/Myr, respectively. Further assuming that the dolerite clast with the highest ^{3}He concentration (15-

420   ROB-028-COL) has been exposed at the drift surface for the longest period, and has therefore experienced mainly

421   surface weathering rather than exhumation from till, we propose that ~2 cm/Myr is likely a maximum limit on rock

422   surface erosion rates for dolerite surfaces in our study area. The assumption that this clast has been exposed at the

423   surface is supported by the fact that 15-ROB-028-COL is a boulder, while the rest of the dolerite surfaces we sampled

424   on Southwest Col are cobbles. If the deposit is younger than 14.5 Ma, an even lower erosion rate would be implied.

425   Although this is an extremely low surface weathering rate by global standards, it is nonetheless consistent with the

426   polar desert climate and the field observations described in section 3.1.3 (i.e., angular clasts with surface varnish and

427   minimal pitting).

3.2.3 Information about geomorphic processes from multiple-nuclide measurements

429   As on Southwest Col, we also measured multiple nuclides (^{10}Be and ^{21}Ne, and, in one case, ^{26}Al) in several sandstone

430   boulders on the Ringleader, WIN, MON, AND, and NLO moraines at Lower Roberts (Figure 11). Although sandstone

431   clasts are rare on these moraines, these data provide some insight into the exposure history of these boulders that we

432   can use to assess the importance of inheritance and post-depositional disturbance for moraine exposure ages.
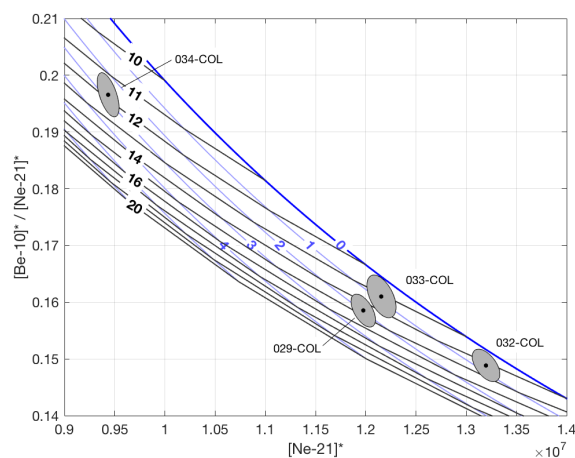
Figure 10. [10]Be-[21]Ne normalized two-nuclide diagram for Southwest Col sandstone erratics. Blue lines are isolines of constant steady erosion (cm/Myr); black lines are isolines of constant exposure age (Ma). The diagram is constructed using LSDn production rate scaling and a [21]Ne/[10]Be production ratio of 4.03 (Balco et al., 2019). Note that the x-coordinate, the [21]Ne concentration normalized to the production rate, is equivalent to the apparent [21]Ne exposure age. Although apparent [21]Ne exposure ages for these samples are 9.5–13 Ma, the two-nuclide diagram shows that the data are better explained by 12–15 Ma exposure at erosion rates between 0.5–3 cm/Myr.

433   In general, a boulder that has experienced a single period of exposure that is equal to the emplacement age of the

434   moraine should display concordant [10]Be, [21]Ne, and [26]Al ages that are the same as those of other boulders on the

435   moraine. For the Ringleader moraine (Figure 11), [10]Be-[21]Ne-[26]Al measurements are concordant at 2.8–3 Ma, therefore

436   consistent with simple exposure at negligible erosion, and lie in the center of the range of [3]He ages from dolerite clasts

437   on the same moraine (Figure 12). These observations suggest that (i) the sandstone boulders have experienced a single

438   period of exposure with minimal post-depositional exhumation or weathering, which is consistent with our field

439   observations as described in section 3.1.1, (ii) their exposure age most likely represents the true emplacement age of

440   the moraine, and (iii) two outliers in the [3]He age distribution can likely be attributed to both inheritance (one ~4 Ma

441   age) and post-depositional disturbance (one ~2 Ma age) .

442   In contrast, paired [10]Be-[21]Ne measurements on four boulders on the MON moraine and one on the WIN moraine

443   (Figure 11), both adjacent to the Bowl and emplaced by ice from upper Roberts overflowing the Bowl headwall (Figure

444   4), display discordant apparent ages. Additionally, apparent exposure ages from both sandstone and dolerite boulders

445   at these moraines are relatively scattered (coefficient of variance > 20%). The [10]Be-[21]Ne data (Figure 11) could be

446   explained either (i) by an extended period of steady erosion at an ice-free site prior to entrainment and deposition of

447   the clasts, or (ii) by repeated exposure and ice cover of the samples prior to emplacement. Both of these conditions

448   are likely if these boulders were sourced from the adjacent outcrop area of sandstone on the Bowl headwall (Figure

449   4a). Thus, we consider it most plausible that the apparent exposure ages of these sandstones reflect prior exposure

450   and, thus, overestimate the true age of the moraine. In general, these results imply that high scatter in exposure ages
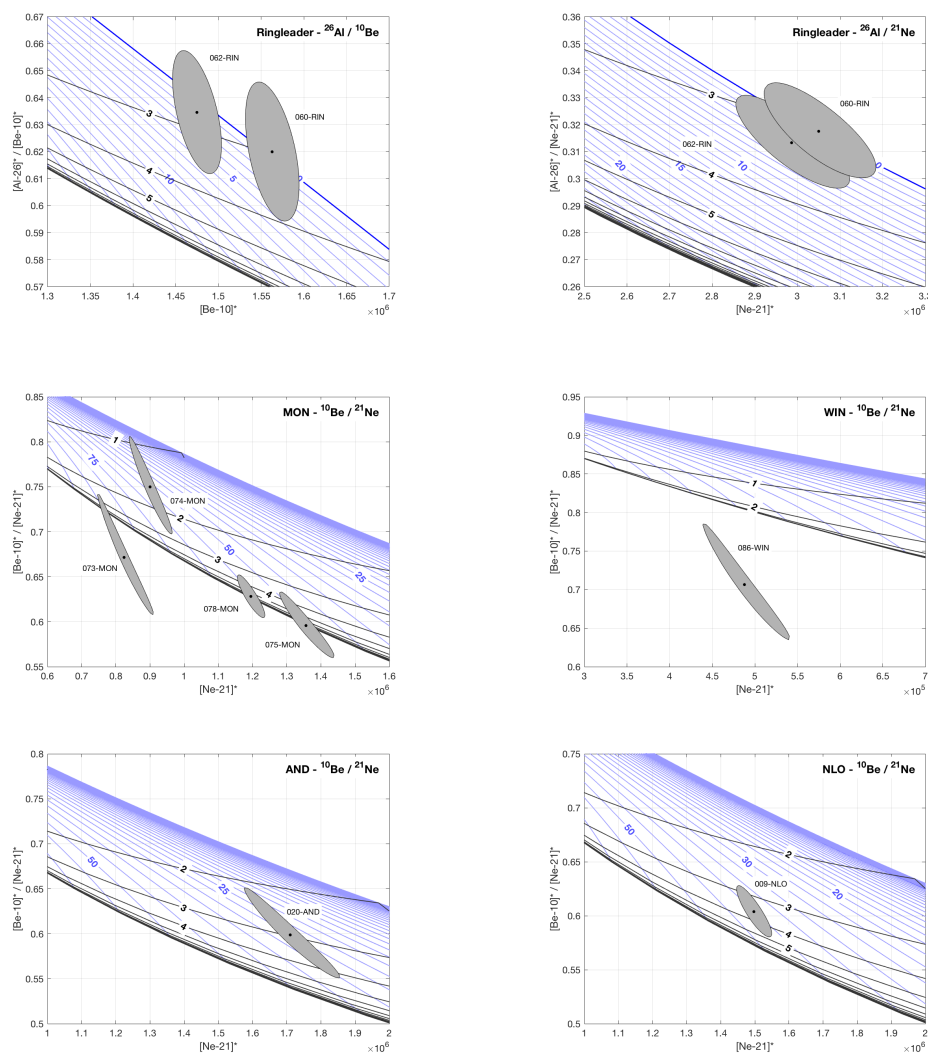
Figure 11. Two-nuclide diagrams for all sandstone erratics collected from lower Roberts Massif moraines. The construction of the diagrams is the same as in Fig. 10. Two-nuclide data for sandstones on the Ringleader moraine lie on the simple exposure line and are in agreement with ^{3}He ages, suggesting that these samples experienced a single period of exposure at negligible erosion, and their apparent ages are a good estimate of the true age of the moraine. On the other hand, paired nuclide data from sandstones on the MON, WIN, AND, and NLO moraines require either significant erosion or a multistage exposure history. An erosion explanation would predict that their apparent ages should be younger than ^{3}He ages on the same moraines; as this is not the case, these samples most likely experienced a multistage exposure history and therefore were emplaced with significant nuclide inheritance.

451   for moraines in the Bowl are most likely explained by inherited nuclide concentrations in clasts sourced from the

452   adjacent headwall, and the true ages of the moraines are therefore likely close to the young end of their age

453   distributions.

454   Finally, paired ^{10}Be-^{21}Ne measurements from the AND and NLO moraines (Figure 11), both at the ice-proximal end

455   of the northern Lower Roberts transect, fall within the "erosion island" on the two-nuclide diagram, indicating that

456   their true exposure ages are older than the apparent ages for either nuclide. In addition, these clasts have apparent ages

457   higher than most ^{3}He ages from these moraines (Figure 12). Again, this is best explained if the scatter exhibited by

458   these moraines is largely the result of inheritance.

459   Overall, although we have a relatively small number of multiple-nuclide data from sandstone boulders, our results

460   demonstrate that (i) inheritance is unequivocally present in some moraine boulders and (ii) inheritance is likely most

461   significant at moraines where boulders are likely sourced from a combination of far-traveled EAIS subglacial debris

462   and cliff fall within the massif itself. These scenarios are also consistent with the observation that boulders on moraines

463   at upper Roberts, which can only be derived from beneath the EAIS, exhibit substantially less scatter than moraines

464   at lower Roberts (Table 1 and Figure 12), where additional input from rockfall is likely. Overall, while none of our

465   observations exclude post-depositional disturbance as a potential source of scatter, they do show that inheritance is

466   likely a more important contributor.

467   **3.3 Outlier Elimination**

468   For each moraine dated, we measured cosmogenic nuclides in 6–8 individual clasts. We observed a variety of

469   distributions ranging from tightly grouped age sets, which likely reflect dispersion due to measurement uncertainties

470   alone, to highly scattered distributions with both old (indicative of nuclide inheritance) and young outliers (e.g., due

471   to subaerial weathering and/or post-depositional disturbance, such as rock toppling or cracking). To interpret these

472   age distributions and arrive at realistic estimates of the moraine age, we utilized constraints from field observations,

473   the stratigraphic ordering of the moraines, exposure-age trends across moraine transects, and measurements of

474   multiple nuclides in various clasts (see above).

475   We first considered geomorphic stratigraphy, weathering characteristics, and trends in exposure-age distributions to

476   identify and eliminate outliers. For Misery Platform, we utilized the cross-cutting relationships of the Misery moraines,

477   which elucidate relative age, to identify exposure ages that are outliers. Although we did not observe such cross-

478   cutting relationships at Upper and Lower Roberts, we exploited the fact that both apparent exposure ages and physical

479   weathering state increase with distance from and elevation above the modern ice margins to determine relative ages

480   of the moraines, and thus to identify likely outliers.

481   We performed an initial screening to remove outliers by assuming that the true depositional age of each moraine lies

482   within the range of measured exposure ages on this moraine. If true, then any exposure ages on one moraine that are

483   older than all exposure ages on a stratigraphically older moraine must be erroneous. Likewise, any exposure ages that

484   are younger than all ages on a stratigraphically younger moraine must also be erroneous. Applying this rule recursively

485   to stratigraphically ordered sets of moraines resulted in the rejection of 46 measurements on 22 boulders (Figures 12

486   and 13; Table S1). We also rejected 9 measurements on 5 boulders as outliers likely resulting from geomorphic

487   processes (i.e., inheritance or post-depositional disturbance), which were not rejected as stratigraphic outliers yet are

488   > 2σ beyond the main age population on that moraine (see Table S1). After this stratigraphic screening was complete,

489   we also rejected as outliers 14 non-concordant ---[10]Be and [21]Ne measurements on 10 sandstone boulders located on

490   the NOLO, AND, WIN, and MON moraines, as those boulders likely contain inherited nuclides (see discussion in

491   Section 3.2.3). In total, we rejected 69 measurements on 37 boulders (Figures 12 and 13; Table S1).

492   The resulting boulder age distributions for each moraine exhibit a variety of forms. Many moraines (e.g., Arena, BAS,

493   Misery B moraines; Figures 12 and 13) display a central cluster approximating a normal distribution, and for these

494   moraines we assign the mean and standard deviation of the ages as the best estimate of the depositional age of the

495   moraine. Other moraines (e.g., SSU, WAL, BGE) showed heavily skewed, bimodal, or scattered age distributions; for

496   these we provide age ranges rather than means in the discussion that follows. In the case of those high-scatter moraines,

497   it is likely that the true moraine age is closer to the younger end of the age range, as we identified inheritance as a

498   more likely contributor to moraine scatter than post-depositional disturbance (Section 3.2.3).

499   **3.4 Moraine ages**

500   In this section, we summarize moraine age estimates assuming zero surface erosion (Table 1; Figures 12 and 13); we

501   discuss the effects of this assumption in later sections.

502   **Lower Roberts:** The oldest dated moraine in the Lower Roberts area – Ringleader –dates to 2.94 ± 0.24 Ma. Along

503   a northward transect from the summit of the Central Rise to the modern ice margin, subsequent moraines yielded the

504   following ages (moraine initials correspond to informal names and sample ID suffixes listed in the ICE-D Antarctica

505   online database; Figure 11): BAS (2.94 ± 0.14 Ma), HDY (2.84 ± 0.08 Ma), WBK (1.62–2.84 Ma), SSU (1.90–2.95

506   Ma), POS (1.16–2.05 Ma), AND (1.08–1.63 Ma), NLO (1.07–1.58 Ma), NLI (0.54–2.09 Ma). A similar transect

507   extending southward from the Central Rise provides the following moraine ages: BBY (1.55–2.69 Ma), BGE (1.41–

508   2.93 Ma), WAL (1.50–2.80 Ma), WIN (0.51–1.00 Ma), MON (0.54 ± 0.01 Ma), and MNM (0.40–0.87 Ma). As

509   discussed in Section 4.2.4, this southern transect displays the highest degree of age scatter, potentially due to the

510   incorporation of rockfall from the surrounding escarpments.

511   **Upper Roberts:** Moraine ages at Upper Roberts display a high degree of internal consistency and are reported here

512   from highest moraine to lowest: Arena (2.64 ± 0.13 Ma); Eine (1.19 ± 0.14 Ma); Kleine (1.18 ± 0.16 Ma); Nacht (1.11

513   ± 0.10); and Musik (0.61–1.10 Ma) (Figure 11). As noted in Section 4.1, undated moraine segments located above the

514   Arena moraine represent higher surface levels of the EAIS, potentially prior to ~2.6 Ma. Additionally, undated

515   moraine segments situated between the Arena and Eine moraines, which differ in elevation by ~45 m, may account

516   for the temporal gap between these two limits.

517   **Misery Moraines:** Approximately 1.5 km southeast of the Southwest Col drift (~14.5 Ma, section 3.2.2), the Misery

518   moraines yielded ages (listed from outermost moraine to innermost) of 7.94 ± 0.23 Ma (Misery D; n = 4), 7.93 ± 0.23

519   Ma (Misery A; n = 1), 7.99 ± 0.06 Ma (Misery B; n = 8), and 7.63 ± 0.29 Ma (Misery C; n = 5) (Figure 12). We

520   consider a young population of ages, between ~4 and 6 Ma, on the Misery A and Misery C moraines to be outliers as

521   the bulk of ages from the complex cluster around 8 Ma. Due to the excellent internal consistency of these age

522   populations, we consider it unlikely that the 8 Ma population reflects inheritance, as that mechanism typically

523   introduces considerable scatter to the data set (Balco, 2011).

Table 1. Roberts Massif moraine and drift ages and statistics.

Site	Elevation (m)	Count (samples exluded)	Age Range of Raw Data (Ma)	Mean Age (Ma)[1]	Age Range (Ma)[2]	Coefficient of Variance (%)	Reduced χ^2
Misery Platform							
Southwest Col	2377	7 (4)	5.20 – 12.86[3]	-	8.63 – 12.86	-	-
Misery D	2249	4 (1)	7.43 – 8.21	7.94 ± 0.23	-	3%	1.00
Misery A	2198	1 (4)	4.34 – 7.93	7.93 ± 0.23	-	'-	'-
Misery B	2252	8 (0)	7.88 – 8.08	7.99 ± 0.06	-	1%	0.07
Misery C	2215	7 (2)	4.70 – 7.96	7.63 ± 0.29	-	4%	1.74
Upper Roberts							
Arena	2303	6 (0)	2.50 – 2.85	2.64 ± 0.13	-	5%	2.49
Eine	2255	5 (2)	0.89 – 2.07	1.19 ± 0.14	-	11%	14.23
Kleine	2241	6 (0)	0.97 – 1.37	1.18 ± 0.16	-	14%	23.74
Nacht	2221	6 (1)	1.03 – 1.52	1.11 ± 0.10	-	9%	6.42
Musik	2215	3 (0)	0.61 – 1.10	-	0.61 – 1.10	30%	184.80
Lower Roberts							
Ringleader	1957	9 (2)	2.16 – 4.07	2.94 ± 0.24	2.57 – 3.37	8%	5.10
Northern Transect							
BAS	1914	7 (0)	2.76 – 3.18	2.94 ± 0.14	2.76 – 3.18	5%	2.52
HDY	1895	5 (2)	2.09 – 3.48	2.84 ± 0.08	2.75 – 2.97	3%	0.90
WBK	1877	6 (1)	1.62 – 3.66	-	1.62 – 2.84	22%	81.95
SSU	1872	7 (0)	1.90 – 2.95	-	1.90 – 2.95	15%	28.78
POS	1865	8 (0)	1.16 – 2.05	-	1.16 – 2.05	21%	48.23
AND	1830	6 (3)	0.89 – 1.66	-	1.08 – 1.63	15%	24.88
NLO	1829	6 (2)	1.07 – 1.58	-	1.07 – 1.58	19%	36.07
NLI	1832	4 (3)	0.54 – 2.09	-	0.54 – 1.39	36%	373.32
Southern Transect							
BBY	1905	5 (0)	1.55 – 2.69	-	1.55 – 2.69	25%	68.30
BGE	1906	6 (1)	1.41 – 4.12	-	1.41 – 2.93	27%	157.67
WAL	1896	7 (0)	1.50 – 2.80	-	1.50 – 2.80	23%	69.22
WIN	1818	7 (2)	0.38 – 1.00	-	0.51 – 1.00	20%	76.27
MON	1791	2 (8)	0.53 – 1.38	0.54 ± 0.01	-	2%	0.24
MNM	1774	4 (3)	0.40 – 1.85	-	0.40 – 0.87	33%	166.30

[1] Used for moraines with age distributions close to normal, and/or a coefficient of variance <15%

[2] Used for moraines with non-normal (scattered) age distributions which have a coefficient of variance >15%

[3] Four youngest ages, obtained from [10]Be measurements, are near saturation and thus not considered.

[4] Population statistics only presented for moraines·

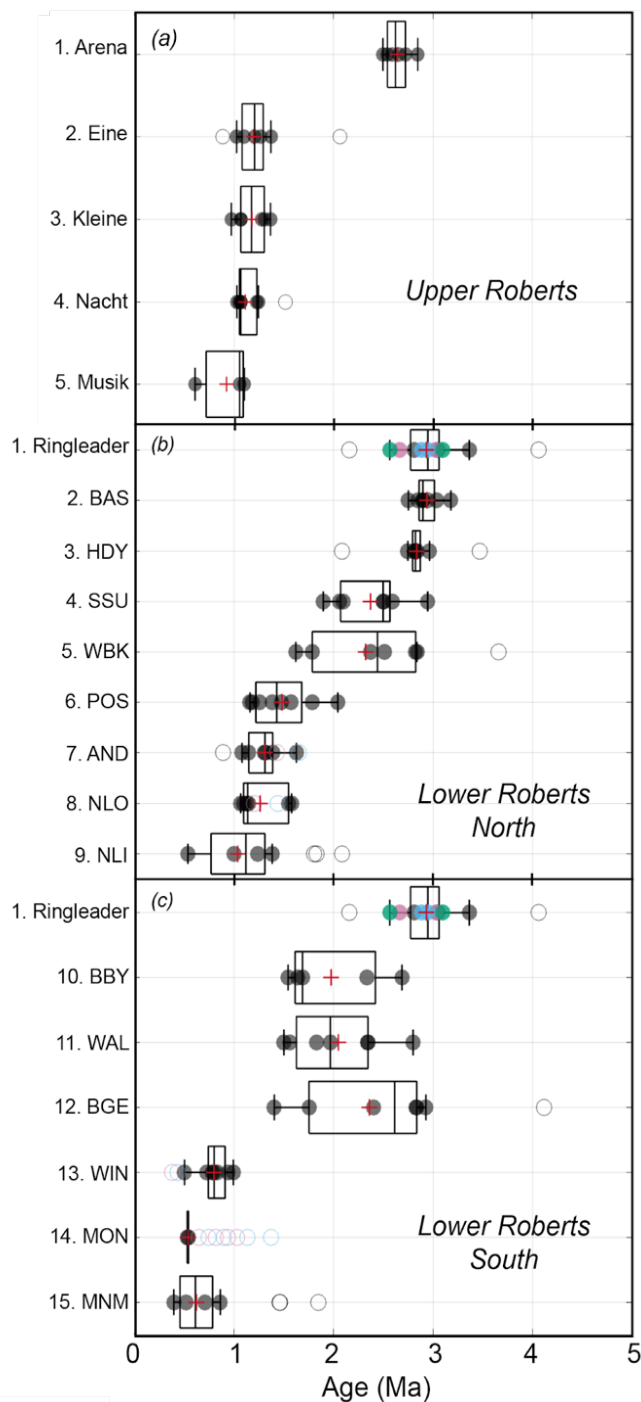[5] All boulders but one are considered outliers on Misery A·

Figure 12: Boxplots showing moraine ages for the Plio-Pleistocene part of the Roberts Massif record. Moraines for each site (Upper Roberts and Lower Roberts northern and southern transects) are listed in stratigraphic order, with the outermost moraine at the top of each panel. Moraine numbers in (a) correspond to those in Figure 7, while moraine numbers in (b) and (c) correspond to those in Figure 4. The Ringleader moraine is shown in both panels (b) and (c), as it is the uppermost moraine in both Lower Roberts transects. [3]He ages are black, [21]Ne ages are blue, [10]Be ages are pink, and [26]Al ages are green. Outliers are shown as open circles. The average moraine age is denoted by a red plus symbol.
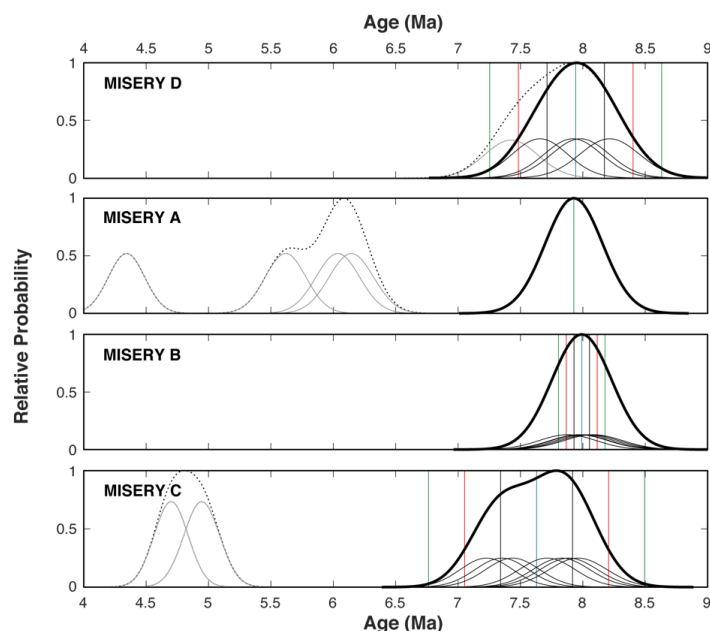
Figure 13: Camel plots (i.e., normal kernel density functions) for the four Misery moraines. The arithmetic mean of the reduced dataset is denoted by the blue line, while the 1σ, 2σ, and 3σ uncertainty envelopes are shown in black, red, and green, respectively. Dotted black lines show the summed probability distributions for the full dataset, including outliers shown in gray, while the thick black lines show the probability distribution for the reduced dataset.

4 Discussion

Cosmogenic-exposure ages on moraines and glacial drift at Roberts Massif afford unprecedented insight into Late Cenozoic variability of the EAIS. The record begins at ~14.5 Ma (Southwest Col drift), while distinct ice-marginal positions date to ~8 Ma and between ~3–1 Ma. As described in Section 4.1, all moraines are characteristic of cold-based glacial conditions and are oriented sub-parallel to the modern EAIS margins, suggesting ice configuration similar to today and the buttressing presence of grounded ice in the Ross Sea Embayment (e.g., Alonso et al., 1992; Bromley et al., 2010; Hauptvogel and Passchier, 2012). In the following sections, we discuss the length of the Roberts Massif glacial-geologic record and address the climatic implications of our findings.

4.1 Uplift at Roberts Massif

Relative to previous glacial-geologic archives from Antarctica, the Roberts Massif record is exceptionally long (~14.5 Ma). At all three sites described in Section 4, moraine age increases with distance from and elevation above the modern

535   EAIS, with the oldest site (Misery Platform) ostensibly indicating the thickest ice. One hypothesis to explain the age-
536   elevation relationship at Roberts Massif is that, while the massif itself has remained isostatically stable for duration of
537   our record, the surface elevation of the EAIS during glacial maxima has lowered systematically over time.
538   Alternatively, the configuration of the EAIS during glacial maxima has remained roughly constant for the duration of
539   the record, but the underlying bedrock has undergone uplift due to tectonism, dynamic topography, and/or isostasy,
540   processes relevant to the millions-of-years timescale. Tectonic uplift at Roberts Massif since ~15 Ma likely was
541   minimal; apatite fission thermochronology in the central TAM suggests that major faulting due to tectonism was
542   complete by ~30 Ma (Fitzgerald, 1994; Miller et al., 2010). However, over the last 3 Myr, approximately 40 m of
543   uplift at Roberts Massif may be attributed to dynamic topography (Austermann et al., 2015), though this value cannot
544   account fully for the ~3 Ma ice positions situated ~170 m (Ringleader moraines) and ~180 m (Arena moraine) higher
545   than the modern EAIS at Lower and Upper Roberts, respectively.

546   Instead, isostatic rebound resulting from deepening of outlet glacier troughs (i.e., removal of rock and replacement by
547   less dense ice) may account for much of the apparent moraine elevation loss through the Roberts Massif record. While
548   large portions of EAIS outlet glaciers, including Shackleton Glacier, are likely frozen to the bed, and thus minimally
549   erosive, regions of these glaciers are thick enough to be at the pressure melting point today (Golledge et al., 2014),
550   and thus eroding their beds. Removal of several hundred meters of rock since the mid-Miocene would therefore result
551   in isostatic rebound of a few hundred meters (Wateren et al., 1999). Although we cannot quantify total trough erosion
552   over the course of our record, this magnitude of uplift is consistent with the observed elevational offset between relict
553   moraines and the modern EAIS.

554   As well as elucidating deposition age, near-saturation concentrations of ^{10}Be on Southwest Col (15-ROB-033-COL)
555   and ^{26}Al the Ringleader moraine (16-ROB-062-RIN) afford maximum-limiting values for isostatic uplift at Roberts
556   Massif, both since ~14.5 Ma and during the last 3 Myr. For these samples, ^{10}Be and ^{26}Al concentrations become
557   saturated (with respect to LSDn scaling) with erosion rates of ~2.3 g cm^{-2} Myr^{-1} and ~7 g cm^{-2} Myr^{-1}, respectively. If
558   we assume that this apparent erosion rate reflects not removal of mass by surface weathering, but rather a decrease in
559   atmospheric depth due to uplift, these erosion rate values provide maximum uplift rates. The ^{10}Be saturation erosion
560   rate for 15-ROB-033-COL yields an uplift rate of ~24 m Myr^{-1} over the last ~14 Myr, indicating that the total
561   maximum uplift over the course of the record is ~350 m, or ~70 m over the last 3 Myr. This estimate accounts for less
562   than half of the elevation difference between the ~3 Ma Ringleader moraine and the EAIS margin (~170 m). In
563   contrast, the ^{26}Al saturation erosion rate for 16-ROB-062-RIN affords a higher uplift rate of ~70 m Myr^{-1} over the last
564   3 Myr, or ~210 m over the Plio-Pleistocene portion of the record, a value that accounts for the full ~170 m elevation
565   difference between the Ringleader moraine and the modern EAIS. Importantly, both the 24 m Myr^{-1} and 70 m Myr^{-1}
566   values each represent maximum uplift rates under the assumption of zero erosion, meaning that the average pace of
567   uplift during the Plio-Pleistocene may not have differed from that during the last ~14.5 Ma. In fact, because ^{26}Al does
568   not quite reach saturation in 3 Myr, it is likely that the 70 m Myr^{-1} is an overestimate. Moreover, the true uplift rate at
569   Roberts Massif probably was lower than those calculated here, since our field observations indicated that some, albeit
570   minor, post-depositional surficial erosion has taken place (Section 3.1).

571   Uplift of ≤ ~200 m over the Plio-Pleistocene is consistent with cosmogenic-nuclide concentrations from the McMurdo

572   Dry Valleys, which indicate minimal vertical change during this period (Brook et al., 1995). Similarly, $^{40}Ar/^{39}Ar$ ages

573   on subaerial volcanic cones limit uplift to 300 m in the Dry Valleys over the past 3 Ma (Wilch et al., 1993) and < 67

574   m in the Royal Society Range over the past 7.8 Ma (Sugden et al., 1999). In contrast, Stern et al. (2005) posit that > 1

575   km of isostatic uplift throughout the central TAM has occurred since 35 Ma due to glacial erosion. If true, the

576   cosmogenic-nuclide concentrations presented here imply that nearly all of this uplift must have taken place between

577   35 and 14 Ma.

578   Given the likelihood of isostatic uplift over the long duration of our record, which potentially accounts for much of

579   the offset between moraine elevations and the modern EAIS, we cannot evaluate changes in ice thickness throughout

580   this ~14 Myr record with certainty. However, we emphasize that a large, cold-based ice sheet with configuration

581   similar to today was present during the dated parts of this record.

582   **4.2 Miocene presence of the EAIS**

583   The oldest dated glacial unit at Roberts Massif, Southwest Col drift, was deposited ~14.5 Ma and demonstrates that

584   the EAIS in the central TAM was cold-based by at least the mid-Miocene (Figure 13). This finding aligns closely with

585   earlier work from the northern TAM that placed the transition to polar conditions at ~14–15 Ma (Denton and Sugden,

586   2005). We note that deposition of Southwest Col drift also coincided broadly with a mid-Miocene climatic shift

587   documented in the Olympus Range, McMurdo Dry Valleys, where well-preserved terrestrial and lacustrine fossils

588   interbedded with ash fall deposits have been interpreted as reflecting an 8°C cooling of Antarctic summers at ~14.5

589   Ma (Lewis et al., 2008). In addition, the age of Southwest Col drift, which provides a minimum-limiting age for cold-

590   based glaciation in the central TAM, is approximately coeval with the Mid-Miocene Cooling Transition (~15–13 Ma),

591   marked by a decline in global sea-surface and bottom-water temperatures (Lear et al., 2015) and atmospheric CO_2

592   concentrations (Zhang et al., 2013). Finally, Southwest Col drift affords minimum-limiting age constraint for the

593   underlying Sirius Group till at Roberts Massif and supports previously published surface-exposure data suggesting

594   that these temperate deposits are > 5 Ma (Ivy-Ochs et al., 1995; Schaefer et al., 1999).

595   Overlying Southwest Col drift, the ~8 Ma Misery moraines represent the oldest ice-marginal landforms identified at

596   Roberts Massif and suggest the presence of a large, cold-based ice sheet at that time. This EAIS configuration is

597   broadly coincident with elevated sea-surface temperatures (Herbert et al., 2016) and Antarctic Bottom Water

598   temperatures (Lear et al., 2015), and potentially higher atmospheric CO_2 (Sosdian et al., 2018) relative to the Plio-

599   Pleistocene. Therefore, our record suggests that a substantial EAIS occupied the central TAM at ~8 Ma despite

600   generally warmer-than-present climatic conditions (Figure 14).

601   **4.3 Plio-Pleistocene presence of the EAIS**

602   The majority of moraines in the Roberts Massif record date to ~3–1 Ma, thus documenting the persistence of a large

603   EAIS during the Plio-Pleistocene transition and early Pleistocene (Figure 13). Because the uncertainties in our moraine

604   ages (~0.1–0.5 Ma) exceed the 40-kyr climate cycles dominant during the pre-MPT world, we do not assign moraines

605   to individual climate events, such as Marine Isotope Stages (i.e., Lisiecki and Raymo, 2005; Railsback et al., 2015).

606   Nonetheless, moraines dated to > ~2.5 Ma indicate a large EAIS in the central TAM during times when global

607   temperatures and atmospheric CO_2 were likely higher than today (Willeit et al., 2019).

608   Several moraines at Roberts Massif date to ~3 Ma (Ringleader, ~3 Ma; BAS, ~3 Ma; HDY, ~2.8 Ma; Arena, ~2.6

609   Ma), inviting the question of whether any of these landforms correspond to the Mid-Pliocene Warm Period (MPWP:

610   ~3.3–3.0 Ma), which has garnered attention as a plausible analog for modern anthropogenic warming. The ongoing

611   debate regarding the resilience of the EAIS during the MPWP bears two leading hypotheses: (i) that the EAIS was of

612   similar extent, or potentially larger, than today during the MPWP (e.g., Sugden et al., 1993; Winnick and Caves, 2015)

613   due to increased East Antarctic precipitation under warmer atmospheric conditions (Huybrechts, 1993); and (ii) that

614   the EAIS was significantly smaller than today (Scherer et al., 2016; Webb et al., 1984) as a result of enhanced melting

615   along marine margins (Pollard and DeConto, 2016) and associated structural collapse (Pollard et al., 2015). At Roberts

616   Massif, moraines dating to the MPWP would support the first hypothesis; however, an absence of MPWP moraines

617   neither proves nor disproves the second hypothesis, as geologic evidence for even a slightly smaller EAIS would lie

618   beneath the modern ice sheet surface (Balco, 2015). Below, we address the possibility that any Roberts Massif

619   moraines date to the MPWP, given the uncertainties associated with exposure dating (i.e., erosion, production rate

620   error, and uplift).

621   First, we address the possibility that erosion of boulder surfaces, which acts to remove a portion of the cosmogenic

622   nuclide inventory, yielded erroneously young apparent exposure ages for the Late Pliocene moraines. As shown in

623   Section 3.2.3, concordant ^{10}Be-^{21}Ne-^{26}Al measurements on Ringleader sandstones afford an exposure age of ~3 Ma,

624   consistent with the ^{3}He ages on that moraine, and both sandstone and dolerite boulders appear to have experienced

625   relatively minimal erosion (i.e., angular, minimal pitting and exfoliation; Section 3.1.1). Applying the maximum

626   surface erosion rate for dolerites of 2 cm/Myr, determined using the ^{3}He concentration of 15-ROB-028-COL (Section

627   3.2.2), the average dolerite age on Ringleader is 3.18 Ma and thus within the uncertainty of the apparent moraine age.

628   Together, our field observations and cosmogenic-nuclide measurements suggest that the apparent age of the

629   Ringleader moraine is not erroneously young due to surface erosion. As discussed in Section 4.1, the maximum

630   possible error in moraine age due to uplift is the same as that for erosion, meaning that the inclusion of uplift has no

631   significant impact on moraine age.

632   Next, we explore the potential effect of cosmogenic nuclide production-rate uncertainty on moraine age. The ^{10}Be

633   production rate is accompanied by ~6% error and ^{3}He by ~10% error (Borchers et al., 2016), meaning that the

634   Ringleader moraine could be ~6 % older (with a lower production rate) or younger (with a higher production rate),

635   using the more precise ^{10}Be production rate as a limit (note: ^{10}Be and ^{3}He ages are statistically indistinguishable).

636   However, we can use the boulder with the highest ^{10}Be concentration on Southwest Col (15-ROB-033-COL), which

637   is close to saturation, to provide a lower limit for the ^{10}Be production rate. Applying a production rate ~2% lower than

638   the globally calibrated production rate of Borchers et al. (2016), which we used to calculate the ^{10}Be ages presented

639   here, sample 15-ROB-033-COL becomes oversaturated with respect to LSDn scaling, suggesting that, at most, the

640   Ringleader moraine (the oldest in the Plio-Pleistocene sequence) is no older than ~3 Ma. Conversely, if the true

641   production rate is higher than that of Borchers et al. (2016), it is possible that the Ringleader moraine is up to 6%

642   younger (~2.8 Ma) than reported here. As there are no sandstones on the oldest landform in the Upper Roberts

643   sequence – Arena Moraine (~2.7 Ma) – we assess the full 10% range in ^{3}He production rate. Assuming a 10% reduction

644   in production rate, the Arena moraine could date to ~3 Ma, or the end of the MPWP.

645   In summary, we did not date any moraines unequivocally to the MPWP, suggesting that the EAIS was not significantly

646   larger than today during that time. However, given the dataset presented here, we cannot evaluate further the

647   configuration of the EAIS during the MPWP because evidence for the ice sheet extent during that time lies beneath

648   the modern glacier. Moreover, we note that our moraine chronology lacks landforms dating to the earlier Pliocene (~5

649   Ma), when conditions are thought to have been as warm as during the MPWP (Burke et al., 2018). Nevertheless, our

650   current dataset provides evidence for a large, cold-based EAIS in the central TAM during the Late Pliocene,

651   immediately following the MPWP, and in the early-to-mid Pleistocene.

5 Conclusions

653   Surficial deposits characteristic of cold-based glaciation at Roberts Massif span the Last Glacial Maximum to Mid-

654   Miocene, thereby providing an exceptionally long geologic record of glaciation for the central TAM. The preservation

655   of numerous, vertically offset ice-marginal deposits is most plausibly explained by the persistence of an EAIS similar

656   in configuration to today during multiple glacial maxima, accompanied by gradual isostatic uplift of Roberts Massif.

657   Coupled with extremely low erosion rates (<< 5 cm/Myr), the prevalence of cold-based deposition over the last ~14.5

658   Ma supports persistent polar desert climate conditions in East Antarctica since the mid-Miocene. Our record also

659   provides minimum-limiting age control for the underlying Sirius Group deposits, suggesting that at least some of the

660   temperate glacial deposits preserved in the TAM are older than 14.5 Ma.

661   Although the Roberts Massif record is not a direct measure of East Antarctic ice volume, our dataset indicates that the

662   EAIS was not any larger during the late Pliocene-early Pleistocene than it was during parts of the Miocene, even

663   though temperatures cooled progressively through the Plio-Pleistocene. Nonetheless, the absence at Roberts Massif

664   of ice-marginal deposits dating unequivocally to the MPWP highlights a critical area for continued investigation, since

665   distal paleoclimate evidence and model simulations suggest the EAIS was smaller than present at that time. Accepting

666   that geologic evidence for even a slightly smaller EAIS during the MPWP would lie beneath the modern ice sheet, we

667   cannot further evaluate the extent to which the EAIS was smaller during the MPWP with the current data set from

668   Roberts Massif.

669   In summary, the Roberts Massif dataset provides a long-term, terrestrial perspective of ice sheet extent in the central

670   TAM, and shows that the EAIS has been a persistent feature of this region since the mid-Miocene. Throughout this

671   record, the EAIS has maintained a configuration similar to today, which requires grounded ice the Ross Sea

672   Embayment, and by extension, West Antarctica, even during periods when global temperature and atmospheric CO_2

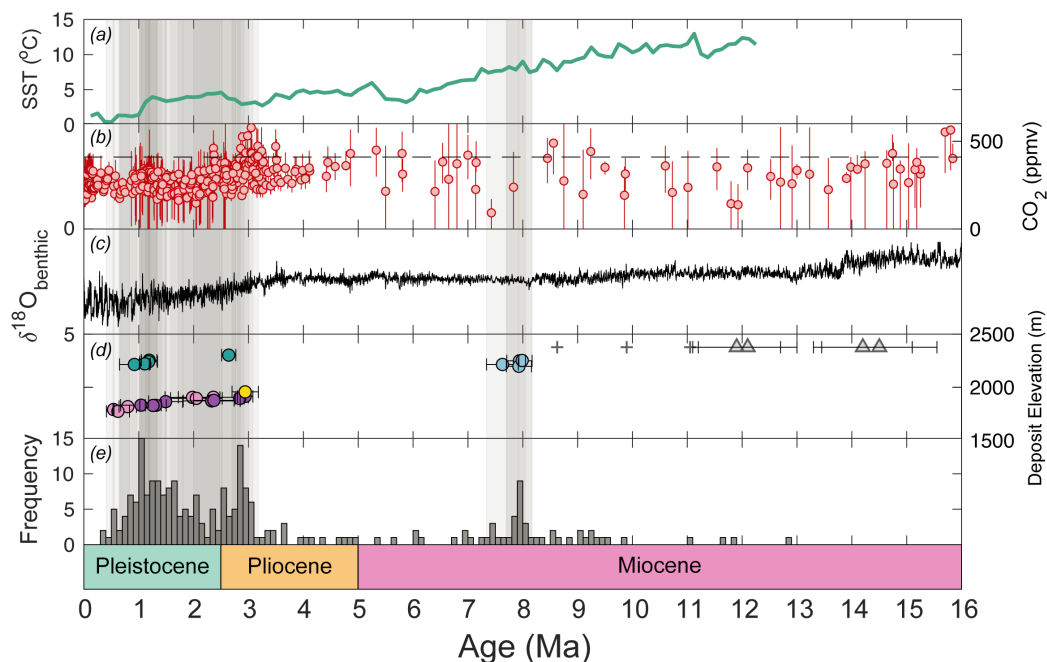673   concentrations likely were similar to or higher than present.

Figure 14: Comparison between Roberts Massif glacial chronology and relevant climate records. (a) Southern Hemisphere alkenone-derived temperature stack (Herbert et al., 2016); (b) Boron-isotope-, paleosol-, and stomata-derived CO_2 records (Beerling et al., 2009; Breecker and Retallack, 2014; Da et al., 2019; Dyez et al., 2018; Ji et al., 2018; Sosdian et al., 2018; Wang et al., 2015; Zhang et al., 2013) (d) benthic oxygen isotope stack (De Vleeschouwer et al., 2017), (e) Moraine age and uncertainty at Roberts Massif, plotted against deposit elevation. Note that deposition of the Misery moraines required ice to be > 300 m thicker than today, which is not reflected in the moraine elevation. Blue circles are the Misery moraines, teal circles are Upper Roberts moraines, the yellow circle is the Ringleader moraine, purple circles are moraines in the Lower Roberts northern transect, pink circles are moraines in the Lower Roberts southern transect, gray plus signs are apparent ages of dolerite boulders of the Southwest Col Drift, and gray triangles are the age of the Southwest Col sandstones, accounting for erosion, (f) Histogram of all apparent exposure ages at Roberts Massif, including outliers. Colors on the timescale at the bottom correspond to moraine colors in Figures 4, 7, and 8. Vertical gray bars denote moraine ages, including uncertainty. Darker gray color shows a higher frequency of moraines.

674   **Data Availability**

675   All analytical information associated with cosmogenic-nuclide measurements appear in the supplementary tables.

676   Analytical information, with additional sample documentation and photographs, is also available in the ICE-

677   D:ANTARCTICA online database (http://antarctica.ice-d.org/).

Author Contribution

679 All authors conducted fieldwork, sample collection, and sample preparation for cosmogenic-nuclide analyses. Balco,
680 Balter and Thomas carried out cosmogenic noble gas measurements, and were responsible for data reduction and
681 analysis. Balter prepared the manuscript with contributions from Balco and Bromley.

Competing Interests

683 The authors declare that they have no conflict of interest.

Acknowledgements

References

694 Ackert, R. P.: Antarctic glacial chronology : new constraints from surface exposure dating., Ph.D. thesis, Woods
695   Hole Oceanographic Institution, Massachusetts Institute of Technology, United States of America, 213 pp.,
696   2000.

697 Ackert, R. P. and Kurz, M. D.: Age and uplift rates of Sirius Group sediments in the Dominion Range, Antarctica,
698   from surface exposure dating and geomorphology, Glob. Planet. Change, 42, 207–225, 2004.

699 Alonso, B., Anderson, J. B., Diaz, J. I. and Bartek, L. R.: Pliocene-Pleistocene Seismic Stratigraphy of the Ross Sea:
700   Evidence for Multiple Ice Sheet Grounding Episodes, Contrib. to Antarct. Res. III, 57, 93–103, 1992.

701 Atkins, C. B.: Geomorphological evidence of cold-based glacier activity in South Victoria Land, Antarctica, Geol.
702   Soc. London, Spec. Publ., 381(1), 299–318, doi:10.1144/SP381.18, 2013.

703 Atkins, C. B., Barrett, P. J. and Hicock, S. R.: Cold glaciers erode and deposit: Evidence from Allan Hills,
704   Antarctica, Geology, 30(7), 659–662, doi:10.1130/0091-7613(2002)030<0659:CGEADE>2.0.CO;2, 2002.

705   Austermann, J., Pollard, D., Mitrovica, J. X., Moucha, R., Forte, A. M., DeConto, R. M., Rowley, D. B. and Raymo,
706   M. E.: The impact of dynamic topography change on antarctic ice sheet stability during the mid-pliocene
707   warm period, Geology, 43(10), 927–930, doi:10.1130/G36988.1, 2015.

708   Balco, G.: The absence of evidence of absence of the East Antarctic Ice Sheet, Geology, 43(10), 943–944,
709   doi:10.1130/focus102015.1, 2015.

710   Balco, G.: Saturated Surfaces in Antarctica: www.cosmognosis.wordpress.com/2016/09/09/saturated-surfaces-in-
711   antarctica/, last access: 15 February 2020, 2016.

712   Balco, G. and Shuster, D. L.: 26Al-10Be-21Ne burial dating, Earth Planet. Sci. Lett., 286(3–4), 570–575,
713   doi:10.1016/j.epsl.2009.07.025, 2009a.

714   Balco, G. and Shuster, D. L.: Production rate of cosmogenic 21Ne in quartz estimated from 10Be, 26Al, and 21Ne
715   concentrations in slowly eroding Antarctic bedrock surfaces, Earth Planet. Sci. Lett., 281(1–2), 48–58,
716   doi:10.1016/j.epsl.2009.02.006, 2009b.

717   Balco, G., Stone, J. O., Lifton, N. A. and Dunai, T. J.: A complete and easily accessible means of calculating surface
718   exposure ages or erosion rates from 10Be and 26Al measurements, Quat. Geochronol., 3, 174–195,
719   doi:10.1016/j.quageo.2007.12.001, 2008.

720   Balco, G., Blard, P. H., Shuster, D. L. and Stone, J. O. H.: Cosmogenic and nucleogenic 21Ne in quartz in a 28-
721   meter sandstone core from the McMurdo Dry Valleys, Antarctica, Quat. Geochronol., 52, 63–76, 2019.

722   Beerling, D. J., Fox, A. and Anderson, C. W.: Quantitative uncertainty analyses of ancient atmospheric co2
723   estimates from fossil leaves, Am. J. Sci., 309, 775–787, doi:10.2475/09.2009.01, 2009.

724   Blard, P. H. and Farley, K. A.: The influence of radiogenic 4He on cosmogenic 3He determinations in volcanic
725   olivine and pyroxene, Earth Planet. Sci. Lett., 276, 20–29, doi:10.1016/j.epsl.2008.09.003, 2008.

726   Blard, P. H., Balco, G., Burnard, P. G., Farley, K. A., Fenton, C. R., Friedrich, R., Jull, A. J. T., Niedermann, S.,
727   Pik, R., Schaefer, J. M., Scott, E. M., Shuster, D. L., Stuart, F. M., Stute, M., Tibari, B., Winckler, G. and
728   Zimmermann, L.: An inter-laboratory comparison of cosmogenic 3He and radiogenic 4He in the
729   CRONUS-P pyroxene standard, Quat. Geochronol., 26, 11–19, doi:10.1016/j.quageo.2014.08.004, 2015.

730   Borchers, B., Marrero, S., Balco, G., Caffee, M., Goehring, B., Lifton, N., Nishiizumi, K., Phillips, F., Schaefer, J.
731   and Stone, J.: Geological calibration of spallation production rates in the CRONUS-Earth project, Quat.
732   Geochronol., 31, 188–198, doi:10.1016/j.quageo.2015.01.009, 2016.

733   Breecker, D. O. and Retallack, G. J.: Refining the pedogenic carbonate atmospheric CO2 proxy and application to
734   Miocene CO2, Palaeogeogr. Palaeoclimatol. Palaeoecol., 406, 1–8, doi:10.1016/j.palaeo.2014.04.012,
735   2014.

736   Bromley, G. R. M., Hall, B. L., Stone, J. O., Conway, H. and Todd, C. E.: Late Cenozoic deposits at Reedy Glacier,
737   Transantarctic Mountains: implications for former thickness of the West Antarctic Ice Sheet, Quat. Sci.
738   Rev., 29(3–4), 384–398, doi:10.1016/j.quascirev.2009.07.001, 2010.

739   Bromley, G. R. M., Winckler, G., Schaefer, J. M., Kaplan, M. R., Licht, K. J. and Hall, B. L.: Pyroxene separation
740   by HF leaching and its impact on helium surface-exposure dating, Quat. Geochronol., 23, 1–8,
741   doi:10.1016/j.quageo.2014.04.003, 2014.

742   Brook, E. J., Kurz, M. D., Ackert Jr., R. P., Denton, G. H., Brown, E. T., Raisbeck, G. M. and Yiou, F.: Chronology
743   of Taylor Glacier Advances in Arena Valley, Antarctica, Using in Situ Cosmogenic 3He and 10Be, Quat.
744   Res., 39, 11–23, 1993.

745   Brook, E. J., Brown, E. T., Kurz, M. D., Ackert, R. P., Raisbeck, G. M. and Yiou, F.: Constraints on Age, Erosion,
746   and Uplift of Neogene Glacial Deposits in the Transantarctic-Mountains Determined From in-Situ
747   Cosmogenic Be-10 and Al-26, Geology, 23(12), 1063–1066, doi:10.1130/0091-7613(1995)0232.3.CO;2,
748   1995.

749   Brown, E. T., Edmond, J. M., Raisbeck, G. M., Yiou, F., Kurz, M. D. and Brook, E. J.: Examination of surface
750   exposure ages of Antarctic moraines using in situ produced 10Be and 26Al, Geochim. Cosmochim. Acta,
751   55, 2269–2283, doi:10.1016/0016-7037(91)90103-C, 1991.

752   Bruno, A. L., Baur, H., Graf, T., Schlkhter, C., Signer, P. and Wieler, R.: Dating of Sirius Group tillites in the
753   Antarctic Dry Valleys with cosmogenic 3He and 21Ne, Earth Planet. Sci. Lett., 147, 37–54,
754   doi:http://dx.doi.org/10.1016/S0012-821X(97)00003-4, 1997.

755   Burke, K. D., Williams, J. W., Chandler, M. A., Haywood, A. M., Lunt, D. J. and Otto-Bliesner, B. L.: Pliocene and
756   Eocene provide best analogs for near-future climates, Proc. Natl. Acad. Sci. U. S. A., 115(52), 13288–
757   13293, doi:10.1073/pnas.1809600115, 2018.

758   Burnard, P. G. and Farley, K. A.: Calibration of pressure-dependent sensitivity and discrimination in Nier-type noble
759   gas ion sources, Geochemistry, Geophys. Geosystems, 1, doi:10.1029/2000GC000038, 2000.

760   Da, J., Zhang, Y. G., Li, G., Meng, X. and Ji, J.: Low CO2 levels of the entire Pleistocene epoch, Nat. Commun., 10,
761   1–9, doi:10.1038/s41467-019-12357-5, 2019.

762   Denton, G. H. and Sugden, D. E.: Meltwater features that suggest Miocene ice-sheet overriding of the Transantarctic
763   Mountains in Victoria Land, Antarctica, Geogr. Ann., 87 A(1), 67–85, 2005.

764   Denton, G. H., Sugden, D. E., Marchant, D. R., Hall, B. L. and Thomas, I.: East Antarctic Ice Sheet Sensitivity To
765   Pliocene Climatic Change From a Dry Valleys Perspective, Geogr. Ann., 75(4), 155–204, 1993.

766   Dyez, K. A., Hönisch, B. and Schmidt, G. A.: Early Pleistocene Obliquity-Scale pCO2 Variability at ~1.5 Million
767   Years Ago, Paleoceanogr. Paleoclimatology, 33(11), 1270–1291, doi:10.1029/2018PA003349, 2018.

768   Fitzgerald, P. G.: Thermochronologic constraints on post-Paleozoic tectonic evolution of the central Transantarctic
769   Mountains, Antarctica, Tectonics, 13(4), 818–836, doi:10.1029/94TC00595, 1994.

770   Gasson, E., DeConto, R. M., Pollard, D. and Levy, R. H.: Dynamic Antarctic ice sheet during the early to mid-
771   Miocene, Proc. Natl. Acad. Sci. U. S. A., 113(13), 3459–3464, doi:10.1073/pnas.1516130113, 2016.

772   Gillespie, A. R. and Bierman, P. R.: Precision of terrestrial exposure ages and erosion rates estimated from analysis
773   of cosmogenic isotopes produced in situ, J. Geophys. Res., 100(B12), doi:10.1029/95jb02911, 1995.

774   Goehring, B. M., Muzikar, P. and Lifton, N. A.: Establishing a Bayesian approach to determining cosmogenic
775   nuclide reference production rates using He-3, Earth Planet. Sci. Lett., 481, 91–100,
776   doi:10.1016/j.epsl.2017.10.025, 2018.

777   Golledge, N. R., Marsh, O. J., Rack, W., Braaten, D. and Jones, R. S.: Basal conditions of two Transantarctic
778   Mountains outlet glaciers from observation-constrained diagnostic modelling, J. Glaciol., 60(223), 855–
779   866, doi:10.3189/2014JoG13J131, 2014.

780   Hauptvogel, D. W. and Passchier, S.: Early-Middle Miocene (17-14Ma) Antarctic ice dynamics reconstructed from
781   the heavy mineral provenance in the AND-2A drill core, Ross Sea, Antarctica, Glob. Planet. Change, 82–
782   83, 38–50, doi:10.1016/j.gloplacha.2011.11.003, 2012.

783   Herbert, T. D., Lawrence, K. T., Tzanova, A., Peterson, L. C., Caballero-Gill, R. and Kelly, C. S.: Late Miocene
784   global cooling and the rise of modern ecosystems, Nat. Geosci., 9(11), 843–847, doi:10.1038/ngeo2813,
785   2016.

786   Holbourn, A., Kuhnt, W., Clemens, S., Prell, W. and Andersen, N.: Middle to late Miocene stepwise climate
787   cooling: Evidence from a high-resolution deep water isotope curve spanning 8 million years,
788   Paleoceanography, 28(4), 688–699, doi:10.1002/2013PA002538, 2013.

789   Huybrechts, P.: Glaciological Modelling of the Late Cenezoic East Antarctic Ice Sheet: Stability or Dynamism,
790   Geogr. Ann., 75 A, 221–238, 1993.

791   Ivy-Ochs, S., Schluchter, C., Kubik, P. W., Dittrich-Hannen, B. and Beer, J.: Minimum 10Be exposure ages of early
792   Pliocene for the Table Mountain plateau and the Sirius Group at Mount Fleming, Dry Valleys, Antarctica,
793   Geology, 23(11), 1007–1010, doi:10.1130/0091-7613(1995)023<1007:MBEAOE>2.3.CO;2, 1995.

794   Ji, S., Nie, J., Lechler, A., Huntington, K. W., Heitmann, E. O. and Breecker, D. O.: A symmetrical CO_2 peak and
795   asymmetrical climate change during the middle Miocene, Earth Planet. Sci. Lett., 499, 134–144,
796   doi:10.1016/j.epsl.2018.07.011, 2018.

797   Jull, A. J. T., Scott, E. M. and Bierman, P.: The CRONUS-Earth inter-comparison for cosmogenic isotope analysis,
798   Quat. Geochronol., 26, 3–10, doi:10.1016/j.quageo.2013.09.003, 2015.

799   Kaplan, M. R., Licht, K. J., Winckler, G., Schaefer, J. M., Bader, N., Mathieson, C., Roberts, M., Kassab, C. M.,
800   Schwartz, R. and Graly, J. A.: Middle to Late Pleistocene stability of the central East Antarctic Ice Sheet at
801   the head of Law Glacier, Geology, 45(11), 963–966, doi:10.1130/G39189.1, 2017.

802   Kober, F., Alfimov, V., Ivy-Ochs, S., Kubik, P. W. and Wieler, R.: The cosmogenic 21Ne production rate in quartz
803   evaluated on a large set of existing 21Ne-10Be data, Earth Planet. Sci. Lett., 302, 163–171,
804   doi:10.1016/j.epsl.2010.12.008, 2011.

805   Lal, D.: Cosmic ray labeling of erosion surfaces: in situ nuclide production rates and erosion models, Earth Planet.
806   Sci. Lett., 104, 424–439, 1991.

807   Lear, C. H., Coxall, H., Foster, G. L., Lunt, D. J., Mawbey, E. M., Rosenthal, Y., Sosdian, S. M., Thomas, E. and
808   Wilson, P. A.: Neogene ice volume and ocean temperatures: Insights from infaunal foraminiferal Mg/Ca
809   paleothermometry, Paleoceanography, 30, 1437–1454, doi:10.1002/2015PA002833.Received, 2015.

810   Levy, R., Harwood, D., Florindo, F., Sangiorgi, F., Tripati, R., von Eynatten, H., Gasson, E., Kuhn, G., Tripati, A.,
811   Deconto, R., Fielding, C., Field, B., Golledge, N., McKay, R., Naish, T., Olney, M., Pollard, D., Schouten,
812   S., Talarico, F., Warny, S., Willmott, V., Acton, G., Panter, K., Paulsen, T., Taviani, M., Askin, R., Atkins,
813   C., Bassett, K., Beu, A., Blackstone, B., Browne, G., Ceregato, A., Cody, R., Cornamusini, G., Corrado, S.,
814   Del Carlo, P., Di Vincenzo, G., Dunbar, G., Falk, C., Frank, T., Giorgetti, G., Grelle, T., Gui, Z.,
815   Handwerger, D., Hannah, M., Harwood, D. M., Hauptvogel, D., Hayden, T., Henrys, S., Hoffmann, S.,
816   Iacoviello, F., Ishman, S., Jarrard, R., Johnson, K., Jovane, L., Judge, S., Kominz, M., Konfirst, M.,
817   Krissek, L., Lacy, L., Maffioli, P., Magens, D., Marcano, M. C., Millan, C., Mohr, B., Montone, P.,
818   Mukasa, S., Niessen, F., Ohneiser, C., Passchier, S., Patterson, M., Pekar, S., Pierdominici, S., Raine, I.,
819   Reed, J., Reichelt, L., Riesselman, C., Rocchi, S., Sagnotti, L., Sandroni, S., Schmitt, D., Speece, M.,
820   Storey, B., Strada, E., Tuzzi, E., Verosub, K., Wilson, G., Wilson, T., Wonik, T. and Zattin, M.: Antarctic
821   ice sheet sensitivity to atmospheric CO2 variations in the early to mid-Miocene, Proc. Natl. Acad. Sci. U.
822   S. A., 113(13), 3453–3458, doi:10.1073/pnas.1516030113, 2016.

823   Lewis, A. R., Marchant, D. R., Ashworth, A. C., Hedenas, L., Hemming, S. R., Johnson, J. V., Leng, M. J.,
824   Machlus, M. L., Newton, A. E., Raine, J. I., Willenbring, J. K., Williams, M. and Wolfe, A. P.: Mid-
825   Miocene cooling and the extinction of tundra in continental Antarctica, Proc. Natl. Acad. Sci., 105(31),
826   10676–10680, doi:10.1073/pnas.0802501105, 2008.

827   Lifton, N., Sato, T. and Dunai, T. J.: Scaling in situ cosmogenic nuclide production rates using analytical
828   approximations to atmospheric cosmic-ray fluxes, Earth Planet. Sci. Lett., 386, 149–160,
829   doi:10.1016/j.epsl.2013.10.052, 2014.

830   Lisiecki, L. E. and Raymo, M. E.: A Pliocene-Pleistocene stack of 57 globally distributed benthic d18O records,
831   Paleoceanography, 20, 1–17, doi:10.1029/2004PA001071, 2005.

832 Margerison, H. R., Phillips, W. M., Stuart, F. M. and Sugden, D. E.: Cosmogenic 3He concentrations in ancient
833   flood deposits from the Coombs Hills, northern Dry Valleys, East Antarctica: Interpreting exposure ages
834   and erosion rates, Earth Planet. Sci. Lett., 230, 163–175, doi:10.1016/j.epsl.2004.11.007, 2005.

835 Mayewski, P. A.: Glacial geology and late Cenozoic history of the Transantarctic Mountains, Antarctica., Ph.D.
836   Thesis, Institute of Polar Studies, The Ohio State University, United States of America, 1975.

837 Mercer, J. H.: Some observations on the glacial geology of the Beardmore Glacier area, Antarct. Geol. Geophys.,
838   (427–433), 1972.

839 Middleton, J. L., Ackert, R. P. and Mukhopadhyay, S.: Pothole and channel system formation in the McMurdo Dry
840   Valleys of Antarctica: New insights from cosmogenic nuclides, Earth Planet. Sci. Lett., 355–356, 341–350,
841   doi:10.1016/j.epsl.2012.08.017, 2012.

842 Miller, K. G., Kominz, M. A., Browning, J. V., Wright, J. D., Mountain, G. S., Katz, M. E., Sugarman, P. J.,
843   Cramer, B. S., Christie-Blick, N. and Pekar, S. F.: The phanerozoic record of global sea-level change,
844   Science, 310, 1293–1298, doi:10.1126/science.1116412, 2005.

845 Miller, S. R., Fitzgerald, P. G. and Baldwin, S. L.: Cenozoic range-front faulting and development of the
846   Transantarctic Mountains near Cape Surprise, Antarctica: Thermochronologic and geomorphologic
847   constraints, Tectonics, 29(1), 1–21, doi:10.1029/2009TC002457, 2010.

848 Nishiizumi, K.: Preparation of 26Al AMS standards, Nucl. Instruments Methods Phys. Res. Sect. B Beam Interact.
849   with Mater. Atoms, 223–224, 388–392, doi:10.1016/j.nimb.2004.04.075, 2004.

850 Nishiizumi, K., Imamura, M., Caffee, M. W., Southon, J. R., Finkel, R. C. and McAninch, J.: Absolute calibration of
851   10Be AMS standards, Nucl. Instruments Methods Phys. Res. Sect. B Beam Interact. with Mater. Atoms,
852   258, 403–413, doi:10.1016/j.nimb.2007.01.297, 2007.

853 Pagani, M., Liu, Z., Lariviere, J. and Ravelo, A. C.: High Earth-system climate sensitivity determined from Pliocene
854   carbon dioxide concentrations, Nat. Geosci., 3, 27–30, doi:10.1038/ngeo724, 2010.

855 Phillips, F. M., Argento, D. C., Balco, G., Caffee, M. W., Clem, J., Dunai, T. J., Finkel, R., Goehring, B., Gosse, J.
856   C., Hudson, A. M., Jull, A. J. T., Kelly, M. A., Kurz, M., Lal, D., Lifton, N., Marrero, S. M., Nishiizumi,
857   K., Reedy, R. C., Schaefer, J., Stone, J. O. H., Swanson, T. and Zreda, M. G.: Quaternary Geochronology
858   The CRONUS-Earth Project : A synthesis, Quat. Geochronol., 31, 119–154, 2016.

859 Pollard, D. and DeConto, R. M.: Contribution of Antarctica to past and future sea-level rise, Nature, 531, 591–597,
860   doi:10.1038/nature17145, 2016.

861 Pollard, D., DeConto, R. M. and Alley, R. B.: Potential Antarctic Ice Sheet retreat driven by hydrofracturing and ice
862   cliff failure, Earth Planet. Sci. Lett., 412, 112–121, doi:10.1016/j.epsl.2014.12.035, 2015.

863 Prentice, M. L., Denton, G. H., Lowell, T. V, Conway, H. C. and Heusser, L. E.: Pre-late Quaternary glaciation of
864   the Beardmore glacier region, Antarctica, Antarct. J. United States, 21, 95–98, 1986.

865   Railsback, L. B., Gibbard, P. L., Head, M. J., Voarintsoa, N. R. G. and Toucanne, S.: An optimized scheme of
866   lettered marine isotope substages for the last 1.0 million years, and the climatostratigraphic nature of
867   isotope stages and substages, Quat. Sci. Rev., 111, 94–106, doi:10.1016/j.quascirev.2015.01.012, 2015.

868   Rovere, A., Raymo, M. E., Mitrovica, J. X., Hearty, P. J., O'Leary, M. J., Inglis, J. D., Leary, M. J. O. and Inglis, J.
869   D.: The Mid-Pliocene sea-level conundrum: Glacial isostasy, eustasy and dynamic topography, Earth
870   Planet. Sci. Lett., 387, 27–33, doi:10.1016/j.epsl.2013.10.030, 2014.

871   Scambos, T. A., Haran, T. M., Fahnestock, M. A., Painter, T. H. and Bohlander, J.: MODIS-based Mosaic of
872   Antarctica (MOA) data sets: Continent-wide surface morphology and snow grain size, Remote Sens.
873   Environ., 111, 242–257, doi:10.1016/j.rse.2006.12.020, 2007.

874   Schaefer, J. M., Ivy-Ochs, S., Wieler, R., Leya, I., Baur, Denton, G. H. and Schluchter, C.: Cosmogenic noble gas
875   studies in the oldest landscape on Earth: surface exposure age of the Dry Valleys, Antarctica, Earth Planet.
876   Sci. Lett., 167, 215–226, 1999.

877   Schaefer, J. M., Denton, G. H., Kaplan, M., Putnam, A., Finkel, R. C., Barrell, D. J. A., Andersen, B. G., Schwartz,
878   R., Mackintosh, A., Chinn, T. and Schlüchter, C.: High-frequency Holocene glacier fluctuations in New
879   Zealand differ from the northern signature, Science, 324, 622–625, doi:10.1126/science.1169312, 2009.

880   Scherer, R. P., DeConto, R. M., Pollard, D. and Alley, R. B.: Windblown Pliocene diatoms and East Antarctic Ice
881   Sheet retreat, Nat. Commun., 7, 1–9, doi:10.1038/ncomms12957, 2016.

882   Seki, O., Foster, G. L., Schmidt, D. N., Mackensen, A., Kawamura, K. and Pancost, R. D.: Alkenone and boron-
883   based Pliocene pCO2 records, Earth Planet. Sci. Lett., 292, 201–211, doi:10.1016/j.epsl.2010.01.037, 2010.

884   Shevenell, A. E., Kennett, J. P. and Lea, D. W.: Middle Miocene ice sheet dynamics, deep-sea temperatures, and
885   carbon cycling: A Southern Ocean perspective, , doi:10.1029/2007GC001736, 2008.

886   Sosdian, S. M., Greenop, R., Hain, M. P., Foster, G. L., Pearson, P. N. and Lear, C. H.: Constraining the evolution
887   of Neogene ocean carbonate chemistry using the boron isotope pH proxy, Earth Planet. Sci. Lett., 498,
888   362–376, doi:10.1016/j.epsl.2018.06.017, 2018.

889   Spector, P., Stone, J., Cowdery, S. G., Hall, B., Conway, H. and Bromley, G.: Rapid early-Holocene deglaciation in
890   the Ross Sea, Antarctica, Geophys. Res. Lett., 44(15), 7817–7825, doi:10.1002/2017GL074216, 2017.

891   Stern, T. A., Baxter, A. K. and Barrett, P. J.: Isostatic rebound due to glacial erosion within the Transantarctic
892   Mountains, Geology, 33(3), 221–224, doi:10.1130/G21068.1, 2005.

893   Stone, J. O.: Air pressure and cosmogenic isotope production, J. Geophys. Res., 105(B10), 23753–23,59, 2000.

894   Stone, J. O., Balco, G., Sugden, D. E., Caffee, M. W., Sass, L. C. I., Cowdery, S. G. and Siddoway, C.: Holcene
895   Deglaciation of Marie Byrd Land, West Antarctica, Science, 299(5603), 99–102,
896   doi:10.1126/science.1115233, 2003.

897   Strasky, S., Di Nicola, L., Baroni, C., Salvatore, M. C., Baur, H., Kubik, P. W., Schlüchter, C. and Wieler, R.:
898   Surface exposure ages imply multiple low-amplitude Pleistocene variations in East Antarctic Ice Sheet,
899   Ricker Hills, Victoria Land, Antarct. Sci., 21(1), 59–69, doi:10.1017/S0954102008001478, 2009.

900   Sugden, D. and Denton, G.: Cenozoic landscape evolution of the Convoy Range to Mackay Glacier area,
901   Transantartic Mountains: Onshore to offshore synthesis, Bull. Geol. Soc. Am., 116(7–8), 840–857,
902   doi:10.1130/B25356.1, 2004.

903   Sugden, D. E. ., Marchant, D. R. . and Denton, G. H. .: The Case for a Stable East Antarctic Ice Sheet, Geogr. Ann.
904   Ser. A Phys. Geogr., 75(4), 151–154, 1993.

905   Swanger, K. M., Marchant, D. R., Schaefer, J. M., Winckler, G. and Head, J. W.: Elevated East Antarctic outlet
906   glaciers during warmer-than-present climates in southern Victoria Land, Glob. Planet. Change, 79, 61–72,
907   doi:10.1016/j.gloplacha.2011.07.012, 2011.

908   Todd, C., Stone, J., Conway, H., Hall, B. and Bromley, G.: Late Quaternary evolution of Reedy Glacier, Antarctica,
909   Quat. Sci. Rev., 29(11–12), 1328–1341, doi:10.1016/j.quascirev.2010.02.001, 2010.

910   Vermeesch, P., Balco, G., Blard, P. H., Dunai, T. J., Kober, F., Niedermann, S., Shuster, D. L., Strasky, S., Stuart, F.
911   M., Wieler, R. and Zimmermann, L.: Interlaboratory comparison of cosmogenic ^{21}Ne in quartz, Quat.
912   Geochronol., 26(1), 20–28, doi:10.1016/j.quageo.2012.11.009, 2015.

913   De Vleeschouwer, D., Vahlenkamp, M., Crucifix, M. and Pälike, H.: Alternating Southern and Northern
914   Hemisphere climate response to astronomical forcing during the past 35 m.y, Geology, 45(4), 375–378,
915   doi:10.1130/G38663.1, 2017.

916   Wang, Y., Momohara, A., Wang, L., Lebreton-Anberrée, J. and Zhou, Z.: Evolutionary history of atmospheric CO_2
917   during the late cenozoic from fossilized metasequoia needles, PLoS One, 10(7), 1–15,
918   doi:10.1371/journal.pone.0130941, 2015.

919   Van Der Wateren, F. M., Dunai, T. J., Van Balen, R. T., Klas, W., Verbers, A. L. L. M., Passchier, S. and Herpers,
920   U.: Contrasting neogene denudation histories of different structural regions in the transantarctic mountains
921   rift flank constrained by cosmogenic isotope measurements, Glob. Planet. Change, (23), 145–172, 1999.

922   Webb, P. N., Harwood, D. M., McKelvey, B. C., Mercer, J. H. and Stott, L. D.: Cenozoic marine sedimentation and
923   ice-volume variation on the East Antarctic craton., Geology, 12, 287–291, doi:10.1130/0091-
924   7613(1984)12<287:CMSAIV>2.0.CO;2, 1984.

925   Wilch, T. I., Lux, D. R., Denton, G. H. and McIntosh, W. C.: Minimal Pliocene-Pleistocene uplift of the dry valleys
926   sector of the Transantarctic Mountains: a key parameter in ice-sheet reconstructions, Geology, 21(9), 841–
927   844, doi:10.1130/0091-7613(1993)021<0841:MPPUOT>2.3.CO;2, 1993.

928   Willeit, M., Ganopolski, A., Calov, R. and Brovkin, V.: Mid-Pleistocene transition in glacial cycles explained by
929   declining CO_2 and regolith removal, Sci. Adv., 5(4), 1–8, doi:10.1126/sciadv.aav7337, 2019.

930   Winnick, M. J. and Caves, J. K.: Oxygen isotope mass-balance constraints on Pliocene sea level and East Antarctic

931   Ice Sheet stability, Geology, 43(10), 879–882, doi:10.1130/G36999.1, 2015.

932   Zhang, Y. G. Y. G., Pagani, M., Liu, Z., Bohaty, S. M. S. M. and DeConto, R.: A 40-million-year history of

933   atmospheric CO2, Philos. Trans. R. Soc. A, 371, 1–20, 2013.

934